MDPI

Article

Evolution of Gas-Liquid Two-Phase Flow in an M-Shaped Jumper and the Resultant Flow-Induced Vibration Response

Hongjun Zhu [1,2,*], Youning Hu [3], Tang Tang [2], Chunning Ji [1] and Tongming Zhou [4]

1   State Key Laboratory of Hydraulic Engineering Simulation and Safety, Tianjin University,
    Tianjin 300350, China
2   State Key Laboratory of Oil and Gas Reservoir Geology and Exploitation, Southwest Petroleum University,
    Chengdu 610500, China
3   Offshore Oil Engineering Co., Ltd., Tianjin 300450, China
4   Department of Civil, Environmental and Mining Engineering, The University of Western Australia,
    Crawley, WA 6009, Australia
*   Correspondence: ticky863@126.com

Abstract: The vibration excited by gas-liquid multiphase flow endangers the structural instability and fatigue life of subsea jumpers due to the cyclic behavior. In this paper, the multiphase flow-induced vibration (MFIV) of an M-shaped jumper is numerically investigated using a two-way fluid-structure interaction (FSI) approach. The effect of gas-liquid ratios (β) ranging from 1:1 to 1:5 is examined with a fixed flow velocity of 3 m/s, and the influence of mixture velocity (v_m) in the range 2–6 m/s is evaluated with a gas-liquid ratio of 1:1. The numerical results reveal the detailed flow evolution of the gas-liquid mixture along the jumper. With inflow of slugs, the pattern successively experiences the slug flow, wavy flow, imperfect annular flow, stratified flow, churn flow, wavy flow and imperfect annular flow in the pipe segments when β = 1:1 and v_m = 3 m/s. This development of mixture flow is significantly altered by changing either the gas-liquid ratio or the mixture velocity. In comparison with the flow evolution in a stationary jumper, the pattern in each pipe segment is not been substantially changed due to the limited response amplitude of order of $10^{-3}D$ (D is the outer diameter of the jumper). Due to the complex flow evolution, the pressure acting on the six bends of the jumper fluctuate in multiple frequencies. Nevertheless, the dominant fluctuation frequency is approximately equal to the inflow slug frequency. Moreover, the inflow slug frequency also dominates the in-plane response of the jumper. Both the in-plane and out-of-plane responses of the jumper exhibit spatial-temporal variation characteristics. The most vigorous oscillation occurs at the midspan of the jumper. As β is reduced, the out-of-plane response of the jumper midspan is suppressed while the in-plane response is enhanced. In contrast, both the in-plane and out-of-plane oscillations of the jumper midspan are amplified with the increase of v_m.

Keywords: flow-induced vibration; gas-liquid two-phase flow; flow evolution; jumper

1. Introduction

In offshore oil and gas engineering, a subsea jumper is a crucial pipe connector that transports oil and/or gas production fluids between two subsea components such as wellhead tree, manifold and riser base [1]. Due to the co-existence of internal oil-gas mixture flow and external currents, subsea jumpers are exposed to multiphase flow-induced vibration (MFIV) as well as vortex-induced vibration (VIV). The VIV of submarine pipelines, including straight spanning, catenary risers and subsea jumpers, has attracted wide attention in engineering applications and has been extensively investigated in past decades because of the potential fatigue damage [2]. In contrast, the understanding of the MFIV of a curved spanning such as a subsea jumper is still limited as the associated literature involving both the gas-liquid multiphase flow evolution and the fluid-structure

interaction (FSI) mechanism is scanty [3]. Moreover, the analysis of MFIV can provide a basis for the understanding of the coupling response.

A jumper pipe may have 4–6 bends for continuously adjusting the internal flow direction, and an unsupported horizontal span length with up to 100D (D is the outer diameter of the jumper), typically arranged in an M-shape or inverted U-shaped configuration [4,5]. An M-shaped jumper has higher displacement tolerances than a U-shaped one but is more susceptible to experience the MFIV due to more frequent changes in flow direction and momentum flux [5]. Nevertheless, the M-shaped jumper is widely used in oil and gas stations and river and gully crossings. Gas-liquid two-phase flow may experience a complicated flow pattern evolution in an M-shaped jumper due to the switching between upward/downward vertical and horizontal flows, which possibly involve stratified, wavy, bubbly, slug, churn and annular flow regimes. The numerical simulation conducted by Tamunodienye et al. illustrated the complex gas-liquid flow development through the different pipe segments of an M-shaped jumper [6]. Among the flow patterns, slug flow is considered as problematic because of the spatial-temporal variations of volumetric void fraction and fluid density and the continuous pressure fluctuation [7,8].

Elbows are a vulnerable part of piping systems in erosive environments [9]. The MFIV of pipe bend, as a basic flow-turning element, has been studied by many researchers. Hossain et al. numerically simulated the slug-churn flow-induced force at a 90° pipe bend using the volume of fluid (VOF) method and the k-ε turbulence model, where k and ε are the turbulent kinetic energy and energy dissipation rate, respectively [10]. It was reported that the dominant frequency of force fluctuation decreased and the root-mean-squared (RMS) of force fluctuation increased with the increase of superficial gas velocity while both of them increased with the increase of superficial liquid velocity, indicating that the flow-induced force was related with the gas-liquid ratio as well as the flow velocity. By means of a computational fluid dynamics (CFD) approach, Bakkouch and Minguez numerically observed that the maximum loads were achieved with the passing of gas bubble tails at the pipe bend [11]. Moreover, the dissociation of slugs into smaller scales contributed to an additional excitation for the vibration. Lu et al. pointed out that the pressure fluctuation introduced by slug flow played a dominant role in generating the excessive vibration [4]. Heijden found the fatigue damage of jumpers is sensitive to the slug flow velocity [5]. A vigorous slug-flow induced (SIV) response of a flexible catenary riser was experimentally observed by Zhu et al. through a non-intrusive measurement when long liquid slugs traveled through the riser [12]. Over a wide range of gas-liquid ratios from 1.0 to 4.5, Zhu et al. reported that both the translation velocity of liquid slug as well as the liquid slug length was enlarged with the increased gas-liquid ratio, resulting in the enhanced vibration and multi-mode response [13].

In comparison with a pipe bend, the intricate development of gas-liquid mixture flow in an M-shaped jumper complicates the dynamic behavior. Chica et al. numerically investigated the air-water two-phase flow behavior in an M-shaped jumper and the excited dynamic response using the combination of the finite element analysis (FEA) solver (Abaqus) and the computational fluid dynamics (CFD) solver (Star CCM+) [14]. It was found that slugs were randomly developed in the vertical sections of the jumper and the vigorous response was excited when the slug frequency was close to the fundamental natural frequency. Through two-way fluid-structure interaction (FSI) numerical analysis, Elyyan et al. demonstrated that the slug frequency was a key factor affecting the total fluid force acting on the jumper and the dynamic response [15]. The coincidence of slug recurrence frequency, vibration frequency and structural natural frequency is the cause of resonance response [16]. With the implementation of the coupled three-dimensional CFD of multiphase flow and the transient nonlinear computational structural dynamics (CSD), Jia numerically investigated the SIV response of a jumper and reported that the vibration amplitude was closely related to the flow rate and slug length [17,18]. Pontaza and Menon numerically observed that the flow-induced stress reached the highest value when the gas volumetric void fraction was 55% and the vibration response predominantly occurred

within the jumper configuration plane [19]. Although the aforementioned literature has successively simulated the MFIV of an M-shaped jumper, the underlying physics is far from well understood, particularly for the correlation of gas-liquid two-phase flow development and the spatial-temporal evolution of dynamic behavior.

In this paper, the MFIV of a typical M-shaped jumper with alternating natural gas-oil inflow is numerically investigated with a variety of gas-liquid ratios. The flow evolution in the stationary jumper is also calculated as a baseline to examine the influence of vibration on the internal flow development. The flow characteristics of gas-liquid mixture and the vibration responses of the critical parts of an M-shaped jumper are discussed in terms of the volume void fraction, pressure fluctuation, response displacements and associated frequencies, and the structural stresses. We aim to shed some light on the MFIV of an M-shaped jumper and the correlation between the dynamic behavior and the development of gas-liquid mixtures.

2. Problem Description

As mentioned above, the pure MFIV is investigated in this work without consideration of VIV, providing a basis for the understanding of the coupling of internal flow-induced vibration and external vortex-induced vibration. Therefore, the effects of the added mass and external pressure due to external water depth were not considered in the analyses. A typical M-shaped jumper with all horizontal and vertical segments in the same plane is considered in current work, as depicted in Figure 1. The jumper is a symmetrical and isodiametric tube with six bends connecting the adjacent horizontal and vertical segments. The lengths of inlet upward tube and outlet downward tube are L_1 = 4 m, while the length of each inside vertical tube is L_3 = 6 m. A short horizontal tube of length L_2 = 3 m is used to connect the adjacent inside and outside vertical tubes, while a long horizontal tube of length L_4 = 10 m links the two inside vertical tubes. The curvature radius of the six identical bends is R/D = 2. The thickness of the jumper is 30 mm. The inlet and outlet ends of the jumper are fixed during the flow-induced oscillation, as both ends are connected to flange plates that are basically fixed. The key parameters are summarized in Table 1. As the coordinate defined in Figure 1, the jumper is initially arranged in the *YOZ* plane. Consequently, the vibration in the *YOZ* plane is called in-plane response while the *X*-directional vibration is named as an out-of-plane response in the remainder of this paper. The bends are numbered consecutively from the inlet to the outlet. In addition, ten cross-sections are defined to examine the flow characteristics in different locations. A probe is mounted on the midspan of the jumper, denoted as Probe C.
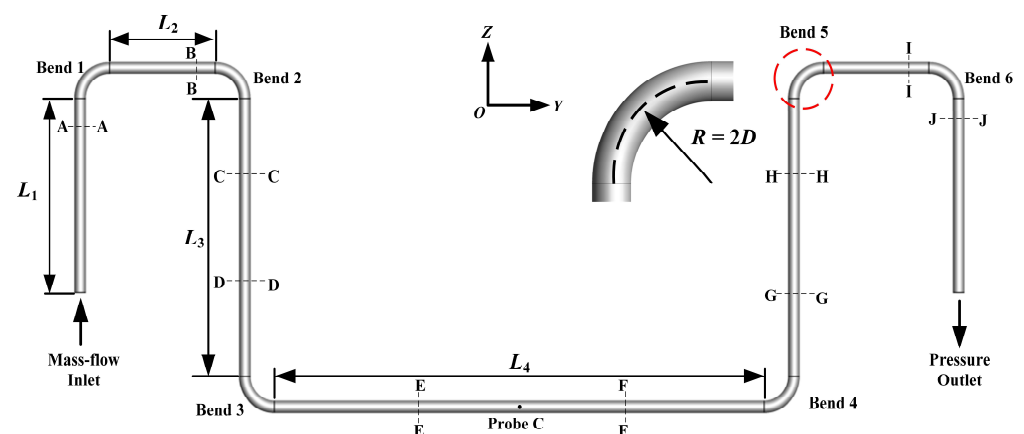

Figure 1. Schematic of the M-shaped jumper with definition of geometric parameters and the locations of monitored cross-sections and probe, where *Z* and *Y* are two coordinate axes, L_1 denotes the length of inlet upward tube, L_2 denotes the length of the top short horizontal tube, L_3 is the length of each inside vertical tube, L_4 is the length of the bottom long horizontal tube, *R* is the curvature radius of bends, *D* is the jumper external diameter, A-A, B-B, C-C, D-D, E-E, F-F, G-G, H-H, I-I and J-J denote the selected cross-sections along the jumper.

Table 1. Key parameters of the M-shaped jumper investigated.

Parameter	Value	Unit
Length of vertical tube in both ends, L_1	4	m
Length of each top horizontal tube, L_2	3	m
Length of each inward vertical tube, L_3	6	m
Length of the bottom tube, L_4	10	m
Internal diameter, d	0.21	m
External diameter, D	0.27	m
Curvature radius of connecting bend, R/D	2	/
Young's modulus, E	2.068×10^{11}	Pa
Poisson's ratio, μ	0.303	/

The economic flow velocities of oil and natural gas transportation are generally in the range of 1–3 m/s and 4–8 m/s, respectively. Therefore, the numerical simulations are conducted in a flow velocity range of 2–6 m/s for the gas-liquid mixture in this work. To produce a stable hydrodynamic slug flow in the jumper inlet, oil and natural gas alternately flow into the jumper with a defined time interval. As listed in Table 2, the gas-to-oil injection time interval ratio T_{gas}/T_{oil} (β) varies from 1:1 to 1:5 when the flow velocity is fixed at 3 m/s. As a consequence, the liquid slug length ranges from 3d (d is the inner diameter of the jumper) to 15d, falling in the typical range 2d–40d for hydrodynamic liquid slugs [20]. Additionally, the flow velocity ranges from 2 m/s to 6 m/s with a constant gas-to-oil injection time interval ratio of β = 1:1. Therefore, nine cases in total are considered in the current work with Reynolds number Re in the range of 1.3×10^4 to 3.9×10^4, where Re is defined as Re = $\rho_m v_m d / \mu_m$ and ρ_m, v_m and μ_m are the density, velocity and dynamic viscosity of the gas-liquid mixture, respectively. This Re range generally belongs to the common range of engineering practice. In each case, the developments of gas-liquid two-phase flow in stationary and vibrating jumpers are calculated separately for comparison. Based on the field parameters, the density and dynamic viscosity of oil are set as 888 kg/m^3 and 0.03135 Pa·s, respectively, and the natural gas at standard room conditions (101,325 Pa and 293.15 K) possesses a density of 0.6679 kg/m^3 and a dynamic viscosity of 1.087×10^{-5} Pa·s. The simulation is conducted with a back pressure of 6 MPa set at the jumper outlet, which is a common medium value in submarine pipeline transportation [21]. Under this operating pressure, the density and dynamic viscosity of natural gas are 44.098 kg/m^3 and 1.217×10^{-5} Pa·s, respectively. As a consequence, the pressure-outlet condition is imposed at the outlet boundary. The mass-flow-inlet condition is specified at the inlet boundary with the consideration of the compressibility of natural gas.

Table 2. Simulation cases.

Case	T_{gas}/T_{oil} (β)	v_{gas} (m/s)	v_{oil} (m/s)
1	1:1	3	3
2	1:2	3	3
3	1:3	3	3
4	1:4	3	3
5	1:5	3	3
6	1:1	2	2
7	1:1	4	4
8	1:1	5	5
9	1:1	6	6

3. Mathematical Model

3.1. Governing Equations

To capture the gas-liquid interface, an interface-tracking model is required. Level Set (LS) and Volume of Fluid (VOF) models are frequently used. The LS function needs to be reinitialized during the iteration, resulting in the non-conservation of mass and an

expensive computing cost [22]. In contrast, the mass is conserved using VOF technique with a relatively low calculation cost. Moreover, VOF has been reported to perform satisfactorily in slug flow [10,23,24]. Thus, the Euler–Euler multifluid VOF model is employed to simulate the compressible natural gas-oil multiphase flow in the M-shaped jumper, where a single set of momentum equations is shared by both phases [10]. The continuity and momentum equations for the gas-liquid mixture are written as follows [25,26]:

$$\frac{\partial \rho_m}{\partial t} + \frac{\partial \rho_m \overline{v_i}}{\partial x_i} = 0 \tag{1}$$

$$\frac{\partial \rho_m \overline{v_i}}{\partial t} + \frac{\partial \rho_m \overline{v_i v_j}}{\partial x_j} = \rho_m g_i - \frac{\partial \overline{p}}{\partial x_i} + \mu_m \nabla^2 \overline{v_i} - \frac{\partial \rho_m \overline{v_i' v_j'}}{\partial x_j} + f_i \tag{2}$$

in which,

$$\rho_m = \alpha \rho_g + (1 - \alpha) \rho_o \tag{3}$$

$$\mu_m = \alpha \mu_g + (1 - \alpha) \mu_o \tag{4}$$

where ρ_m and μ_m are the density and dynamic viscosity of the gas-liquid mixture, respectively, ρ_g and ρ_o are the gas density and oil density, respectively, μ_g and μ_o are the associated dynamic viscosities of gas and oil, α is the gas void fraction, t is the flow time. x_i is the space coordinate in i direction. v_i represents the instantaneous velocity component in i direction—for example v_1, v_2 and v_3 are the velocities in X, Y and Z directions, respectively, while v_i' is the fluctuation velocity component in i direction, g_i is the gravitational acceleration in i direction. p is pressure, f_i is the surface tension force between phases in i direction, and "‾" denotes the time-averaged value of the associated parameter.

Additionally, a volume fraction continuity equation for the gas phase is solved to track the interface between two phases [27]. Note that no phase change and no-slip between gas and liquid are assumed at the interface.

$$\frac{\partial \alpha}{\partial t} + \frac{\partial \alpha \overline{v_i}}{\partial x_i} = 0 \tag{5}$$

The two-equation k-ε model is well-developed and frequently used to treat turbulence. The renormalization-group (RNG) k-ε turbulence model is a refined one, improving the accuracy for rapidly strained flows and swirling flows [28]. Therefore, the RNG k-ε turbulence model is used for closure of the above governing equations [29,30]. The equations of turbulent kinetic energy (k) and its dissipation rate (ε) are written as:

$$\frac{\partial k}{\partial t} + \frac{\partial k \overline{v_j}}{\partial x_j} = \frac{\partial}{\partial x_j}\left[\left(\mu_m + \frac{\mu_t}{\sigma_k}\right)\frac{\partial k}{\partial x_j}\right] - \frac{\partial v_i \overline{v_i' v_j'}}{\partial x_j} - \varepsilon \tag{6}$$

$$\frac{\partial \varepsilon}{\partial t} + \frac{\partial \varepsilon \overline{v_j}}{\partial x_j} = \frac{\partial}{\partial x_j}\left[\left(\mu_m + \frac{\mu_t}{\sigma_\varepsilon}\right)\frac{\partial \varepsilon}{\partial x_j}\right] - C_{\varepsilon 1}\frac{\varepsilon}{k}\frac{\partial v_i \overline{v_i' v_j'}}{\partial x_j} - C_{\varepsilon 2}\frac{\varepsilon^2}{k} - R_\varepsilon \tag{7}$$

in which,

$$\mu_t = C_\mu \rho_m k^2 / \varepsilon \tag{8}$$

$$R_\varepsilon = \frac{C_\mu \eta^3 (1 - \eta / \eta_0) \varepsilon^2}{(1 + \beta_0 \eta^3) k} \tag{9}$$

$$\eta = \frac{k}{\varepsilon}\left[\left(\frac{\partial v_i}{\partial x_j} + \frac{\partial v_j}{\partial x_i}\right)\frac{\partial v_i}{\partial x_j}\right]^{1/2} \tag{10}$$

where μ_t is the turbulent viscosity, R_ε is an extra strain rate term, C_μ, $C_{\varepsilon 1}$, $C_{\varepsilon 2}$, σ_k, σ_ε, η_0 and β_0 are empirical constants, specified as 0.1, 1.44, 1.92, 1.0, 1.3, 4.38 and 0.012, respectively, in the present scheme [28]. The aforementioned flow governing equations are discretized

with the finite volume method (FVM). The pressure-implicit with splitting of operators (PISO) algorithm is used to deal with the coupling between the pressure and flow velocity. A first-order implicit scheme and a second-order upwind scheme are adopted for the temporal discretization and the discretization of convective terms, respectively [31].

In one time step, the flow field and structure response are solved. After obtaining pressure and shear stresses through solving the above flow controlling equations, the fluid forces are substituted into the structural motion equation, which are written in the form of a matrix for the application of the finite element method (FEM):

$$M\left\{\frac{\partial^2 X_i}{\partial t^2}\right\} + C\left\{\frac{\partial X_i}{\partial t}\right\} + K\{X_i\} = \{F_i(t)\} \tag{11}$$

where M is the mass matrix, C is the damping matrix, K is the equivalent stiffness matrix which is converted from the bending stiffness (EI), X_i donates the displacement in i direction and $F_i(t)$ is the hydrodynamic force in i direction, which is computed by performing an integration involving both the pressure and shear stresses on the considered element of the jumper. In the simulation, the jumper with both ends fixed is discretized into n elements, and the motion equation for each element is solved by the Hilber−Hughes−Taylor method [32]. After the response displacement is obtained, the position of the jumper and associated grids are updated accordingly. Then the flow field in the deformed jumper is calculated for the next time step. The time step Δt is set as 0.005 s, ensuring the Courant number below 1.0 in the entire computational domain. The two-way coupling approach is utilized through the multifield solver of the software package ANSYS MFX, in which FLUENT is employed to solve the flow field while the transient structural module is adopted to calculate the structure dynamic behavior. This two-way coupling iteration is conducted until sufficient periodic results (more than 100 cycles) are obtained. In this work, 0.8–2.5 s are required for the appearance of periodic results, and then another 50–60 s are consumed to record the results for statistical analysis.

3.2. Meshing and Dependence Check

As shown in Figure 2, both the fluid and solid domains are divided with structured hexahedron grids. For the fluid domain, the grids of six bends and those close to the jumper wall are refined, considering the adjustment of flow direction and the velocity gradient of boundary layer, respectively. As seen from the mesh of a cross-section, the jumper perimeter is equally discretized with 40 nodes, and the radial size of the first layer of mesh next to the jumper wall is set as $0.0095D$ ($y^+{\sim}10$). The cross section is tessellated with a copper-coin-shaped mesh, where eleven layers are considered in the O-ring region with a radial expansion ratio of 1.2. The axis of each horizontal/vertical tube is evenly divided with elements of height $0.167D$, and the curvature radius of each bend is equally discretized with 39 nodes, ensuring the smooth data transfer between associated tubes and bends. The mesh of the fluid domain is achieved with the sweep of cross-section grids along the jumper axis. The solid domain is tessellated with a four-layer structured mesh, in which the perimeter and length of each segment (horizontal/vertical tubes and bends) are divided with the same nodes as those of the fluid domain for high efficiency of data transfer.
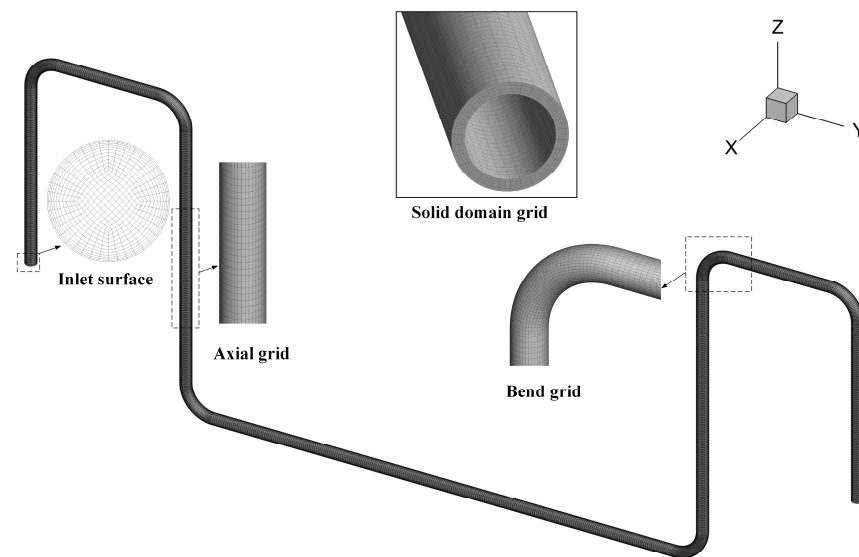
Figure 2. The computational mesh of the whole domain and the zoom-in view of key parts.

A mesh independence check is performed prior to the simulations. The key calculation results obtained by five mesh systems are compared in Table 3, where P_{RMS} and X_{RMS} are the RMS pressure stress acting on the inner surface of associated bend and the RMS displacement of corresponding bend along the X direction, respectively. It is seen that the differences of numerical results become smaller as the number of grids increases, and both P_{RMS} and X_{RMS} converge at M4, as the relative difference between M4 and M5 is less than 1%. Therefore, the mesh resolution of M4 is adopted in the subsequent simulations.

Table 3. Mesh independence validation for the vibrating jumper in case 1.

Mesh	Elements of Fluid Domain	Elements of Solid Domain	P_{RMS} at Bend 2 (Pa)	P_{RMS} at Bend 3 (Pa)	P_{RMS} at Bend 4 (Pa)	X_{RMS} of Bend 2 (mm)	X_{RMS} of Bend 3 (mm)	X_{RMS} of Bend 4 (mm)
M1	201,427	21,360	33,336.94	43,216.98	39,352.24	0.072	0.394	0.444
M2	313,721	41,139	38,114.12 (14.33%)	49,358.11 (14.21%)	45,330.01 (15.19%)	0.083 (14.82%)	0.453 (14.97%)	0.509 (14.53%)
M3	403,958	61,220	41,986.51 (10.16%)	54,205.08 (9.82%)	49,967.27 (10.23%)	0.091 (10.06%)	0.498 (9.93%)	0.559 (9.76%)
M4	512,647	82,098	43,854.91 (4.45%)	56,552.16 (4.36%)	52,470.63 (5.01%)	0.095 (4.93%)	0.525 (5.42%)	0.586 (4.85%)
M5	628,326	101,431	44,039.10 (0.42%)	56,863.19 (0.51%)	52,932.37 (0.88%)	0.096 (0.68%)	0.527 (0.38%)	0.589 (0.53%)

3.3. Modal Analysis and Numerical Validation

The modal analysis is performed to identify the modal shapes and natural frequencies in both in-plane and out-of-plane directions using the ANSYS Modal module without the consideration of the internal fluid mass and external fluid added mass. Figure 3 depicts the fundamental modal shapes of the empty jumper in the three coordinate axes as well as associated 1st natural frequencies. It is seen that the in-plane natural frequencies (f_{y1} and f_{z1}) are approximately double that of the out of plane (f_{x1}), although the two natural frequencies are slightly different in the jumper plane due possibly to the specific size and geometry.
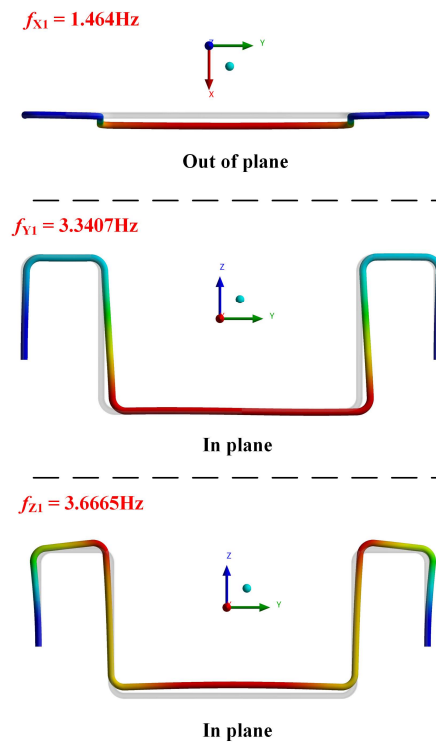
$f_{X1} = 1.464 \text{Hz}$

Out of plane

$f_{Y1} = 3.3407 \text{Hz}$

In plane

$f_{Z1} = 3.6665 \text{Hz}$

In plane

Figure 3. The fundamental modal shapes and associated natural frequencies along the three coordinates, where f_{x1}, f_{y1} and f_{z1} are the first natural frequencies in the three directions.

The employed numerical model is validated against the reported experimental results of an air-water flow-induced vibration of an inverted U-shaped jumper [33]. A high-speed camera was used in that study to capture the flow evolution in the test and laser displacement sensors were employed to record the vibration displacements of the upper right bend in three directions. Figure 4 compares the calculation results through the current numerical model with the reported data. Figure 4a depicts the spatial flow evolution in three instants when hydrodynamic slug flow is injected into the jumper with $v_{air} = 0.51$ m/s and $v_{water} = 0.46$ m/s. Figure 4b plots the variation of vibration displacements with the gas void fraction (φ_{gas}). It is clearly seen that both the two-phase flow regime and the vibration response are in good agreement with the experimental results. Therefore, the present two-way coupling approach could provide an accurate prediction for the MFIV response.
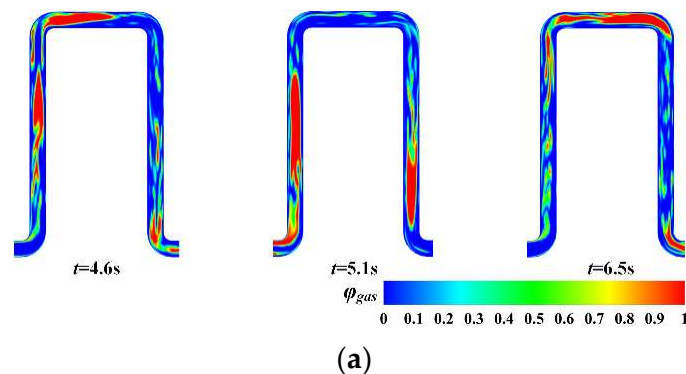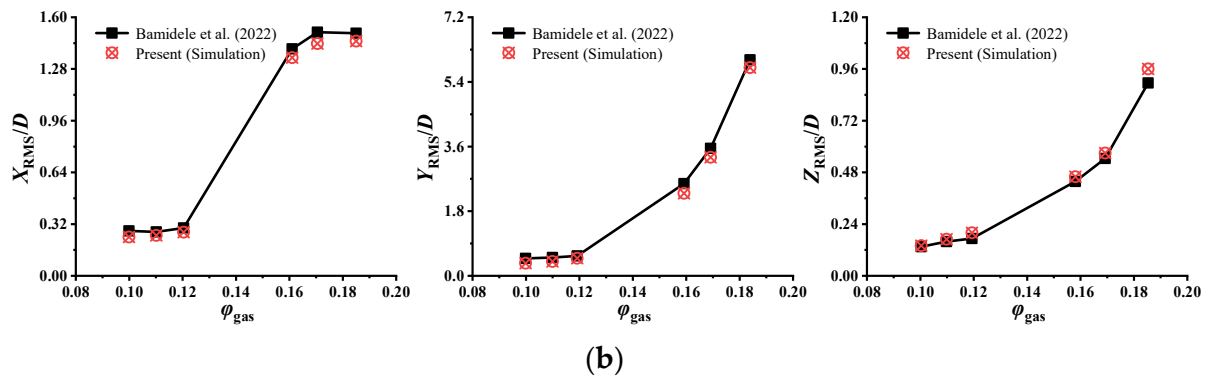
$t=4.6\text{s}$ $t=5.1\text{s}$ $t=6.5\text{s}$

φ_{gas}

0   0.1 0.2 0.3 0.4 0.5 0.6 0.7 0.8 0.9   1

(a)

Figure 4. *Cont.*

(b)

Figure 4. Modal validation test for the gas-liquid flow-induced vibration of an inverted U-shaped jumper, where φ_{gas} is the gas void fraction, X_{RMS}/D, Y_{RMS}/D and Z_{RMS}/D are the root-mean-squared normalized amplitudes in the three directions, and t is the flow time: (**a**) the flow evolution in the inverted U-shaped jumper with $v_{air} = 0.51$ m/s and $v_{water} = 0.46$ m/s; the upper part of this figure is from paper; (**b**) the root-mean-squared displacements of the upper right bend in three directions.

4. Results and Discussion

4.1. Flow Evolution in the Static Jumper and Flow-Induced Force

　　To verify the viability and stability of the definition of alternate inflow boundary condition through user-defined functions (UDF), the variation of mass flow rate in the inlet is monitored during the simulation. As depicted in Figure 5, the mass flow rate switches between 2.94 kg/s and 62.34 kg/s with a time interval of 0.2 s in the standard case (case 1), illustrating the perfect alternate inflow condition. Therefore, stable liquid slugs could be produced in the inlet with an expected length of about 0.6 m, which is demonstrated in Figure 6. Although the oil film thickness is about 4.7 mm on the wall, it does not influence the produced slug length.
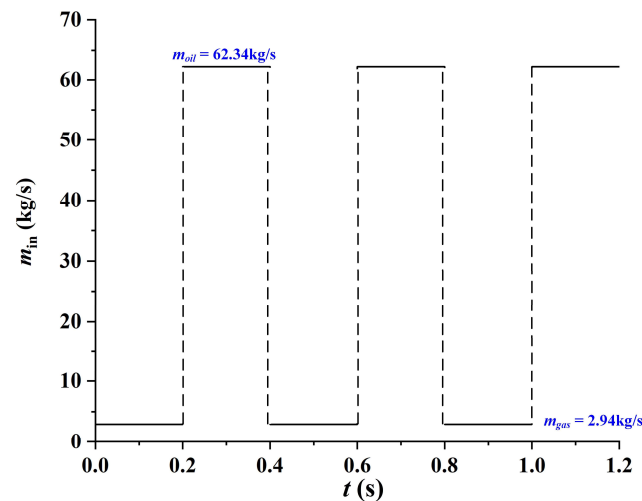

Figure 5. The variation of mass flow rate (m_{in}) monitored in the inlet, taking case 1 as an example, where m_{oil} and m_{gas} are the mass flow rate of oil and gas, respectively.

　　Figure 6 shows the gas-liquid mixture development in the static jumper. The liquid (oil) slugs denoted in red color are produced in the inlet and migrate upward in the first vertical tube. Due to the viscosity effect, the head of the oil slug changes to arc shape while moving upward, suggesting the development of a boundary layer. It is clearly seen that the gas plug is significantly elongated when it is close to the first bend (Bend 1), mainly attributed to the buoyancy caused by density difference. Owing to the participation of centrifugal force, the oil slug is twisted in the first bend. Subsequently, natural gas selectively accumulates at the top of the left horizontal span while oil flows along the tube

bottom, yielding a wavy flow regime. At the second bend (Bend 2), oil is thrown to the extrados because of the inertia action. After that, oil drops rapidly in the downward tube, generally presenting an imperfect annular flow regime. This regime remains in the third bend (Bend 3). Nevertheless, oil droplets accumulate in the bottom of the long horizontal span, quickly generating the stratified flow regime. In the fourth bend (Bend 4), gas and liquid flow along the intrados and extrados, respectively, maintaining the stratified flow. However, the flow pattern becomes irregular in the subsequent upward tube, falling in the churn flow regime. The wavy flow regime reoccurs in the right horizontal span but is relatively unstable in comparison with that in the left horizontal span. Finally, the imperfect annular flow is reproduced in the last vertical downward tube due to the force of gravity. Figure 6a depicts the process of flow replacement at the beginning. After that, the calculation is conducted until sufficient periodic results are obtained. When the gas-liquid mixture flow is well developed, the spatial flow evolution is basically stable, i.e., the flow regime in each pipe segment does not vary over time although the flow is still unsteady, as shown in Figure 6b.
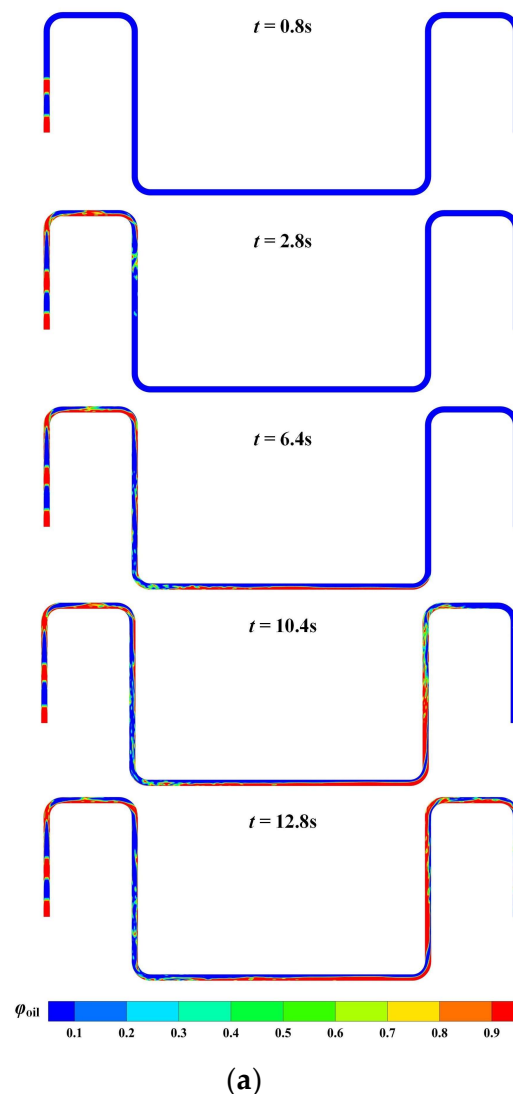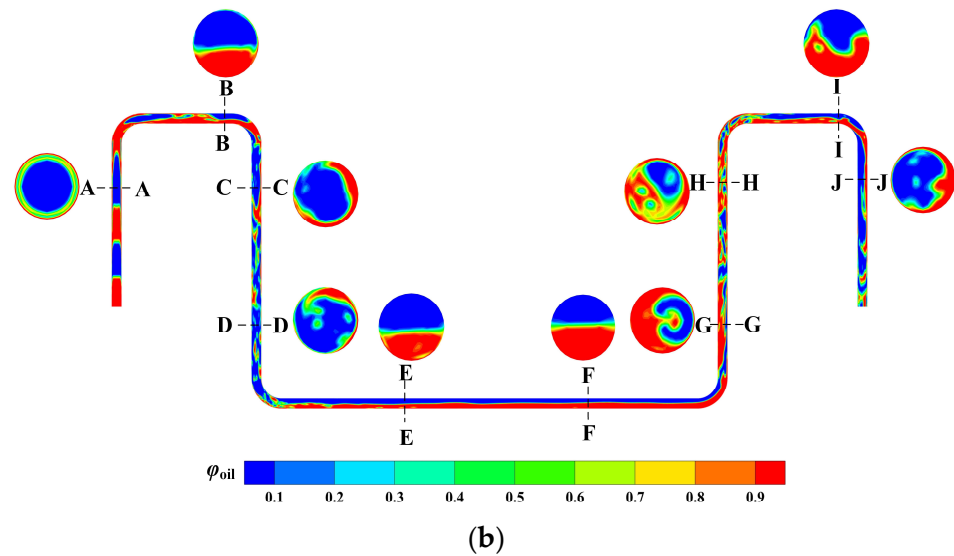

(a)

Figure 6. *Cont.*

(b)

Figure 6. Flow evolution in the static jumper in case 1, where φ_{gas} is the gas void fraction, t is the flow time, and A-A, B-B, C-C, D-D, E-E, F-F, G-G, H-H, I-I and J-J denote the selected cross-sections along the jumper: (**a**) the process of oil-gas mixture transported through the jumper; (**b**) contours of oil volume fraction in considered cross-sections when the periodically stable flow is achieved in the jumper.

As depicted in Figure 7, the gas void fraction fluctuates periodically over time in the monitored cross-sections (taking B-B, D-D, F-F, H-H and I-I, for example), although the flow regimes in specific sections have no variation. These results indicate that the gas-liquid mixture flows through the same cross-section with a periodic recurrence of void fraction. The D-D cross-section possesses the maximum time-averaged void fraction ($\bar{\alpha}$) among the five considered cross-sections, due to the gas accumulation in the center of annular flow. Noted that although D-D cross-section locates at the lower part of the downward tube, oil does not accumulate here and instead gathers in the long horizontal span with the result of stratified flow regime. It explains why the maximum $\bar{\alpha}$ occurs in the D-D cross-section. In contrast, the minimum $\bar{\alpha}$ appears in the H-H cross-section, possibly attributed to the disturbance of oil in the churn flow regime. The time-averaged gas void fractions are approximately equal in B-B and I-I cross-sections because of the same wavy flow regime.
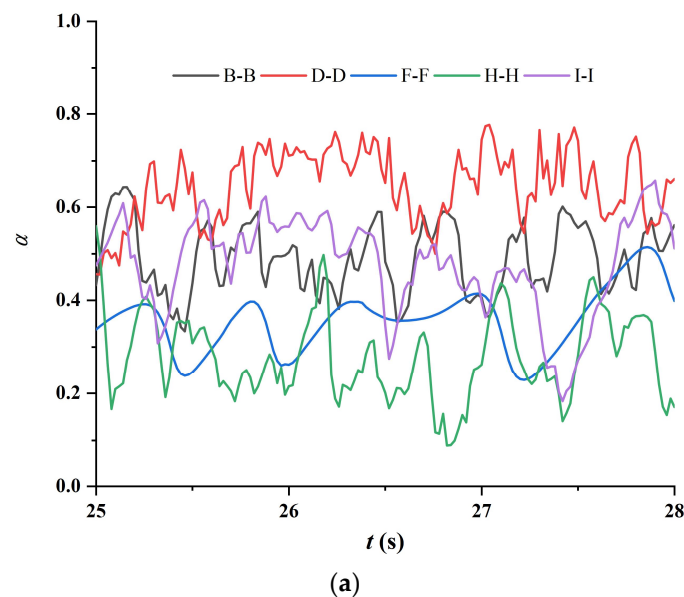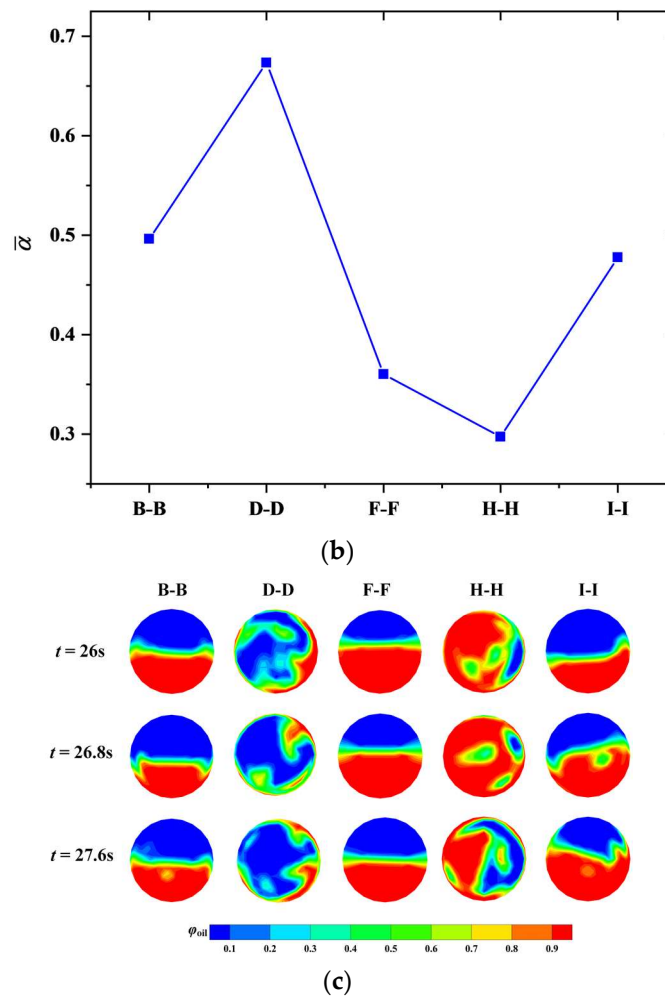

(a)

Figure 7. *Cont.*

(b)

(c)

Figure 7. The gas void fraction at monitored sections of the static jumper in case 1, where φ_{gas} is the gas void fraction, t is the flow time, α is the gas void fraction, $\overline{\alpha}$ is the maximum time-averaged void fraction, and B-B, D-D, F-F, H-H and I-I denote the selected cross-sections along the jumper: (**a**) time histories of gas void fraction; (**b**) time-averaged gas void fraction; (**c**) the contours of oil volume fraction at three instants.

The pressure stresses acting on the inner surface of six bends are compared in Figure 8 for case 1, accompanied by the frequency spectra and wavelet time-varying frequency which is obtained using the wavelet transform. The main difference between a spectrogram and a wavelet transform is that the latter could give the variation of frequency over time. Additionally, the wavelet analysis is a measure of similarity between the basic function and the original function. The wavelet-transform coefficient (weight) calculated indicates how close the function is to the wavelet basic function at the particular scale. Therefore, the wavelet-transform coefficient is a non-dimensional parameter, i.e., there is no unit for the color bar. The third bend (Bend 3) undergoes the maximum pressure stress, due mainly to the impact of falling liquid. The second largest pressure is exerted on the fourth bend (Bend 4), indicating the effect of liquid column weight on this low-position bend. Although Bend 3 and Bend 4 are in the same level, the relatively large pressure at the former signifies the pressure difference that drives the gas-liquid mixture from the left (Bend 3) to the right (Bend 4). This phenomenon of pressure difference also appears between Bend 1 and Bend 2 and between Bend 5 and Bend 6 with a greater pressure acting on the left one. As Bend 6 is close to the outlet, the associated pressure is the minimum one. It is clearly seen that the pressure stresses fluctuate in multiple frequencies for all six bends. The first reason is the multi-frequency fluctuating void fraction, as illustrated in Figure 7. The second reason is that a bend may experience flow pattern transition and space-varying void fraction along

its axis, as depicted in Figure 6. Nonetheless, the dominant frequency is distinguishable from others because the fluctuation energy concentrates in this frequency, as seen from the wave-let frequency contours. Moreover, the six bends present the same dominant frequency of 2.52 Hz, which is approximately equal to the inflow slug frequency of 2.5 Hz (cycle $T = T_{gas} + T_{oil} = 0.4$ s). It implies that the pressure fluctuation is closely related to the inflow condition in spite of the spatial flow evolution. As gas-liquid mixture flows through the jumper, other frequencies participate in the fluctuation with increased allocated energy, suggesting the influence of flow evolution. More unstable wavy flow is generated in the right horizontal span, contributing to the more irregular fluctuation of pressure in comparison with upstream tubes. As a consequence, a secondary frequency of 1.08 Hz is distinctly observed in Bend 6 due to the occurrence of flow evolution from unstable wavy flow to imperfect annular flow.
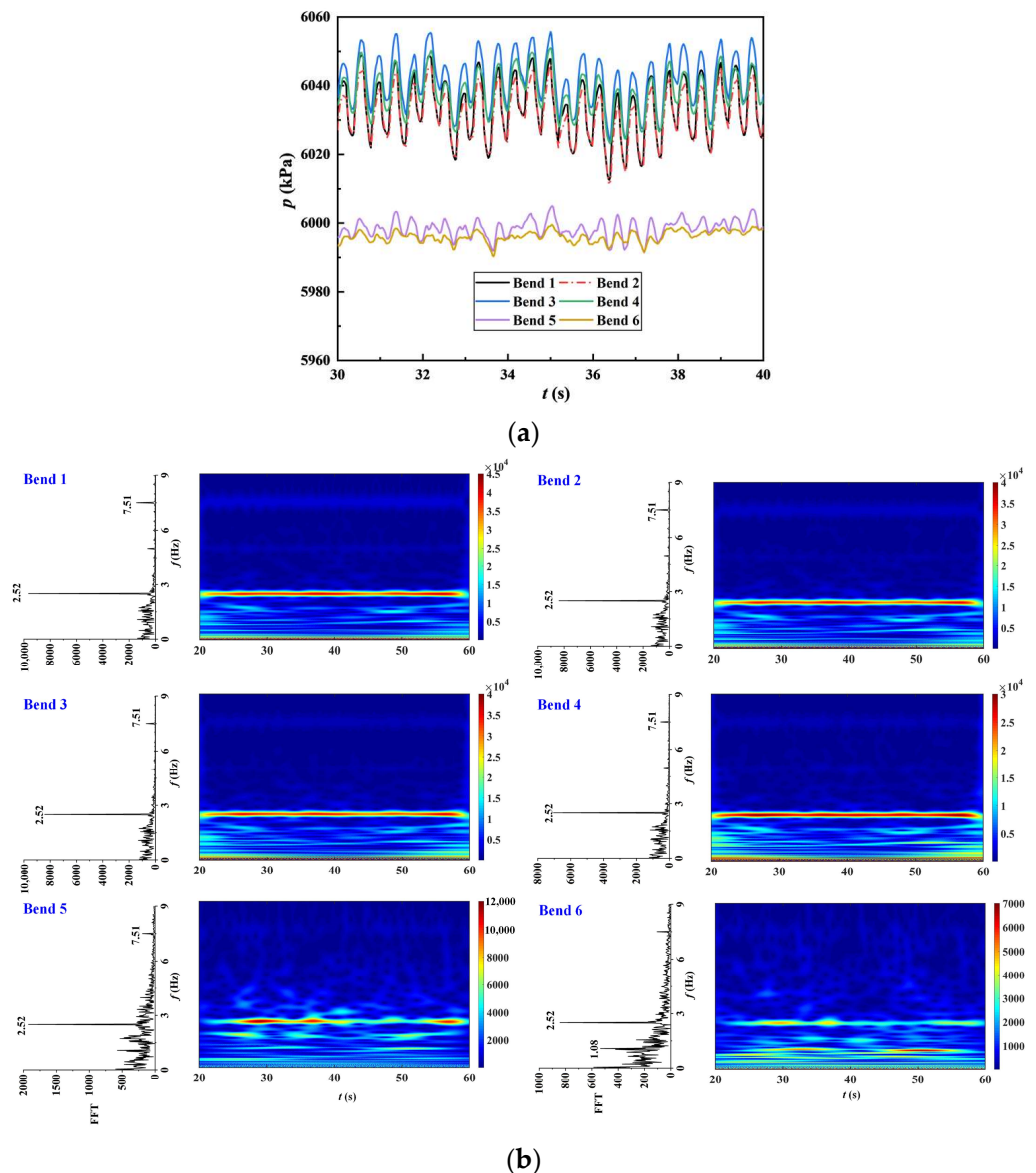

(**a**)

(**b**)

Figure 8. The variation of pressure (*p*) acting on the bends of the static jumper over time in case 1, where *f* is the fluctuation frequency and *t* is the flow time: (**a**) time series of pressure exerted on the bends' surface; (**b**) frequency spectrum of pressure fluctuation.

4.2. Flow-Induced Vibration and Its Influence on Flow Evolution

In this study, the response results apply for a rigid jumper without the consideration of deformation. Figure 9 depicts the time series of the normalized vibration displacements of

six bends and the midspan (Probe C) in the standard case (case 1). It is seen that the vibration response varies spatially along the jumper, presenting different response amplitudes and time-averaged displacements at different locations. The two bends (Bend 1 and Bend 6) close to fixed ends exhibit tiny vertical displacements (Z/D is the normalized vertical displacement), affected by the end constraints. Additionally, the out-of-plane displacements (X/D is the normalized out-of-plane displacement) of these two bends are also limited. In contrast, both Bend 1 and Bend 6 experience distinct horizontal displacements (Y/D is the normalized horizontal displacement) with response amplitude around $0.001D$. This is mainly attributed to the change of momentum flux in the sudden turns. Moreover, the offset directions of the two bends are opposite, i.e., Bend 1 undergoes a positive horizontal oscillation while Bend 6 presents a negative one. The out-of-plane displacement is slightly increased when the location shifts to the other end of associated horizontal span, i.e., when the objective shifts from Bend 1 to Bend 2 or shifts from Bend 6 to Bend 5. This indicates a weakening of the influence of end constraints. Nevertheless, both Bend 2 and Bend 5 experience the vertically downward displacement with obvious amplitude around $0.0015D$. Additionally, a similar response amplitude is observed in the horizontal oscillation for these two bends, which also present the opposite movement direction like Bends 1 and 6. Therefore, the in-plane response becomes distinguishable in Bends 2 and 5. Both the in-plane and out-of-plane responses are obvious for the two bends connecting the bottom horizontal span as well as the midspan (Probe C). Generally, the vibration of Bend 3 is similar to that of Bend 4 in both the time-averaged displacement and response amplitude, and the out-of-plane response is more vigorous than the in-plane one. The maximum time-averaged Z/D is found in Probe C, indicating the greatest downward displacement. In addition, the midspan experiences the maximum out-of-plane amplitude, followed by Bends 3 and 4, as seen from the RMS amplitude curves in the bottom right corner of Figure 9. Therefore, the gas-liquid multiphase flow results in a downward displacement and the vigorous oscillation mainly occurs in the out-of-plane direction of the middle part of this M-shaped jumper. Although the jumper undergoes vibration in both in-plane and out-of-plane directions, the response amplitudes are limited to the order of $10^{-3}D$. It may be noted that the fatigue life is not only related to the response amplitude but also the vibration frequency.

The vibration frequencies of the six bends and Probe C are compared in Figure 10. The out-of-plane oscillation energy concentrates at a single frequency of 1.34 Hz, which is close to the fundamental natural frequency (f_{x1} = 1.464 Hz), for the two bends connecting the bottom horizontal span and Probe C. This indicates the oscillation of the middle horizontal span and the two connected bends is dominated by the fundamental mode. The concentrated energy mainly contributes to the vigorous oscillation, as illustrated in Figure 9. In contrast, the energy is scattered in the other four bends. For Bends 1 and 2 that connect the left horizontal span, the fundamental mode still dominates the out-of-plane response, although a high frequency band emerges. For Bends 5 and 6 that connect the right horizontal span, the high frequency band approximately possesses the same vibration energy of 1.34 Hz. It implies that the vibration is complicated with more intense competition in the pipe segments close to the outlet. Notably, the high frequency band center is around 5 Hz, which is nearly double that of pressure fluctuation frequency and that of inflow slug frequency, suggesting the correlation between the vibration and the gas-liquid mixture flow. In comparison with the out-of-plane response, the in-plane response is dominated by a distinctly peak frequency of 2.51 Hz, which is equal to that of inflow slug frequency. The dominant frequencies in both in-plane and out-of-plane directions are therefore less than the associated fundamental natural frequencies, leading to the 1st order oscillation.
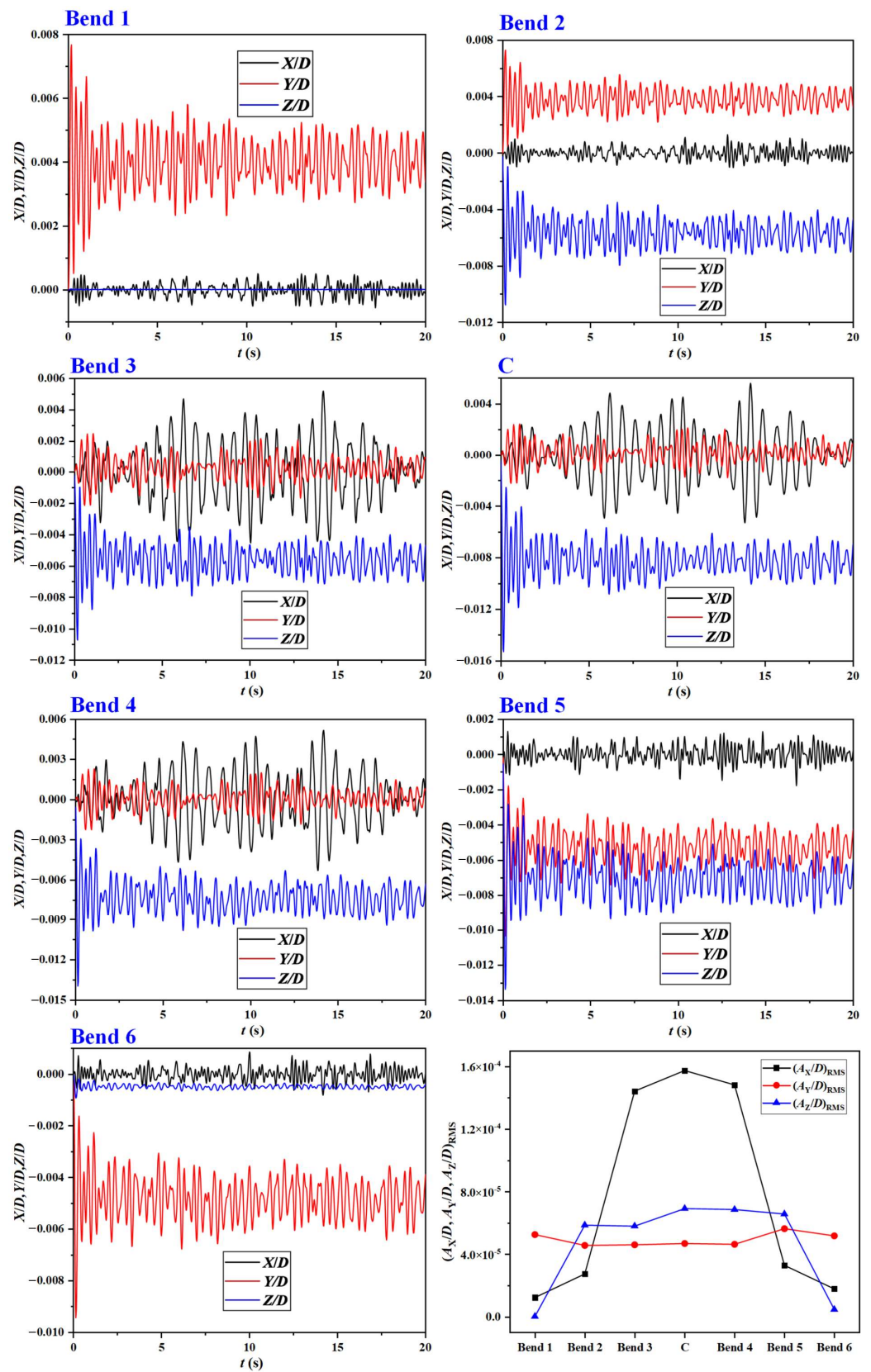
Figure 9. Time series of the normalized vibration displacements of the monitored bends and probe in case 1, where X/D, Y/D and Z/D are the normalized displacements in the three directions, and $(A_X/D)_{RMS}$, $(A_Y/D)_{RMS}$ and $(A_Z/D)_{RMS}$ are the root-mean-squared normalized amplitudes in the three directions.
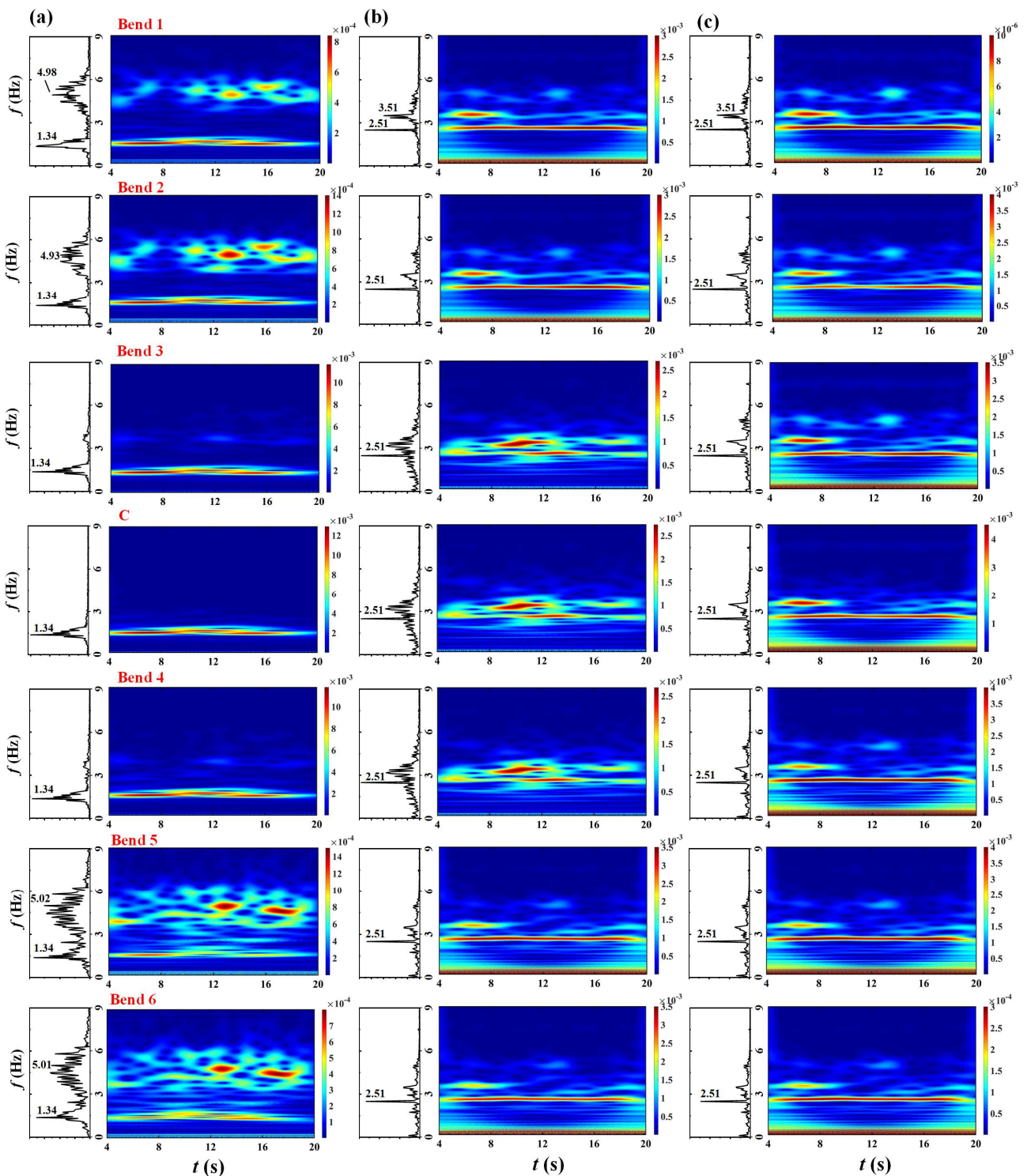
Figure 10. The vibration frequencies of monitored bends and probe in case 1, where *f* is the fluctuation frequency and *t* is the flow time: (**a**) variation of frequency in *X* direction; (**b**) variation of frequency in *Y* direction; (**c**) variation of frequency in *Z* direction.

Apart from the vibration displacement and response amplitude and frequency, the flow-induced stress (Von Mises stress) is a critical parameter that affects service life. Figure 11 depicts the time histories of the stresses of the six bends and the associated maximum values. It is clearly seen that the stresses also experience the periodical fluctuation like that of pressure and void fraction. Unlike the variation of pressure, the bends close to both ends undergo relatively large stresses as a result of the effect of end constraints. The

stress of Bend 4 is the minimum among the six bends, due possibly to the relatively small impact force of stratified flow. Bend 3 experiences the second-smallest stress. The impact force of falling liquid probably contributes to the greater stress in comparison with Bend 4. Among the six bends, the fifth bend (Bend 5) bears the maximum fluctuation amplitude as well as the greatest stress, possibly attributed to the flow transition from churn flow to wavy flow and the fastest flow velocity in the upward tube. Therefore, Bend 5 is a vulnerable component of the oscillating M-shaped jumper.

(a)

(b)
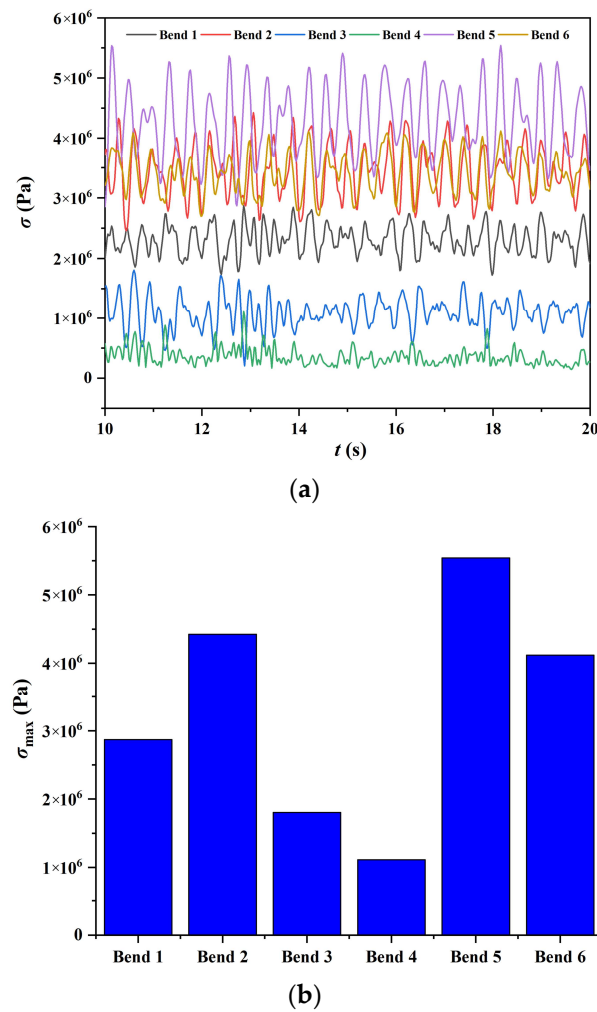
Figure 11. The stresses of monitored bends for the vibrating jumper in case 1, where σ_{max} is the maximum stress, σ is the structural stress, and t is the flow time: (**a**) time series of structural stresses; (**b**) comparison of the maximum stress.

Figure 12 compares the flow evolution in the jumper between the static and vibration conditions. We can see that the flow regime in each pipe segment has no obvious alteration, including the thickness of oil film and the length of liquid slugs. It illustrates that the effect of small-amplitude oscillation on the flow pattern is limited. Nevertheless, the stratified flow is formed faster in the middle horizontal span when the jumper is oscillating. Moreover, the gas-liquid interface is smoother than that in a static jumper. It implies that the downward displacement of the middle horizontal span is of benefit to the stabilization of the gas-liquid mixture. As a consequence, the churn flow in the subsequent upward tube is also stabilized as compared to the static case. Therefore, the influence of vibration response on the mixture flow is mainly reflected in the two pipe segments connecting Bend 4.
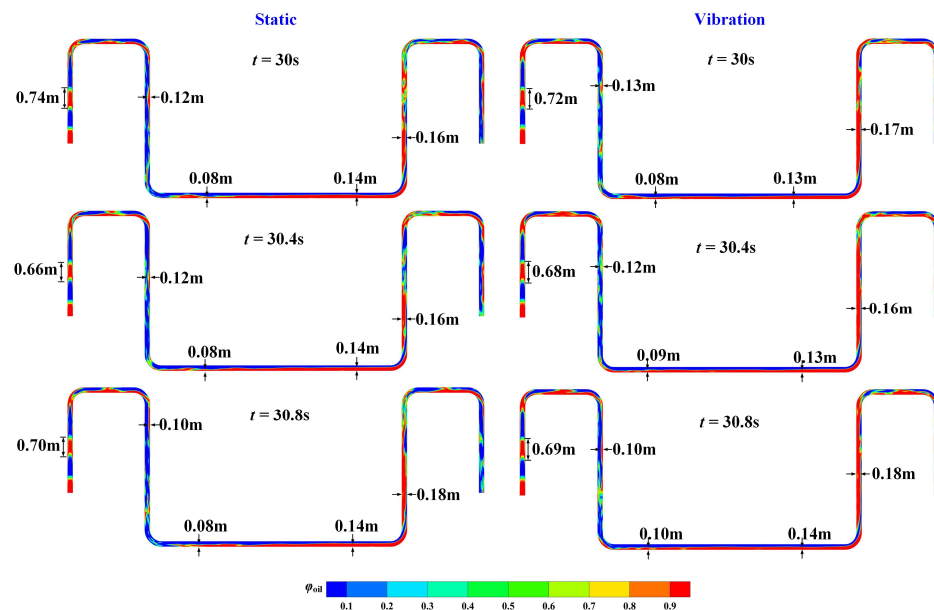
Figure 12. Comparison of the flow regimes in the jumper between the static and vibration conditions for case 1, where φ_{oil} is the volume fraction of oil and t is the flow time.

4.3. Effect of Gas-Liquid Ratio

The results apply for a rigid jumper in spite of the variation of gas-liquid ratio. Figure 13 compares the flow characteristics at different gas-liquid ratios, where the variation of gas-liquid ratio is achieved by extending the inflow time of oil. The flow evolution is significantly altered by changing the gas-liquid ratio. It is clearly seen that the length of liquid slugs in the first upward tube is prolonged with decreasing the gas-liquid ratio (β). Consequently, the liquid slug cloud fills the left horizontal span when $\beta \leq$ 1:4 in spite of the occurrence of gas penetration. As β decreases from 1:1 to 1:5, the flow regime thus evolves from the wavy flow to the aerated slug flow. In the subsequent downward tube, the thickness of oil film grows with reducing β because of the increased oil fraction. When $\beta \leq$ 1:3, the flow pattern shifts from annular flow to churn flow, due possibly to the disturbance induced by the rapid fall of more liquid. In the bottom horizontal span, the height of the oil layer increases as β decreases. At $\beta =$ 1:5, nearly 4/5 of the tube height (a diameter for the horizontal span) is occupied by oil, as seen from the contours in E-E and F-F cross-sections. In the subsequent upward tube, the gas-liquid mixture is stabilized as β reduces, presenting the transition from churn flow to bubbly flow. Accordingly, the wavy flow in the right horizontal span also evolves to bubbly flow as β decreases from 1:1 to 1:5, and the pattern shifts from annular flow to churn flow in the last downward tube.

Due to the increase of oil content in the left downward tube, the impact force acting on the bottom bend (Bend 3) generally becomes greater as β reduces from 1:1 to 1:5, as depicted in Figure 14. Thus, it is reasonable to believe that the excited response varies with β. Figure 15 compares the vibration response of the midspan of the jumper (Probe C) at different gas-liquid ratios. The selection of midspan for analysis here is because its vibration response is the most prominent one as illustrated in the above section. It is seen that the normalized out-of-plane displacement (X/D) is reduced with the decrease of β, owing to the stabilization of stratified flow in the bottom horizontal span. Additionally, the peak frequency has no obvious variation with β because there is no adjustment in the flow regime. In contrast, more than one frequency takes part in the in-plane response when $\beta \leq$ 1:2, and the competition among multiple frequencies becomes more intense as β further reduces. Both the normalized displacements in the two directions of the jumper plane (Y/D and Z/D) are generally increased with the reduction of β. It is mainly attributed to the occurrence of flow turns in the jumper plane and the increased impact force exerted by the gas-liquid mixture flow of increased oil content. Therefore, the midspan of the jumper

experiences the reverse trend in the variation of in-plane oscillation with β as compared to the out-of-plane response. As shown in Figure 16, with the reduction of β from 1:1 to 1:5, the stress of Bend 5 is increased in both the time-averaged value and the fluctuation amplitude. It is mainly attributed to the enhanced in-plane response. Additionally, the fluctuation frequency of stress is consistent with the out-of-plane and vertical response, signifying the close correlation between the vibration and structure stress.
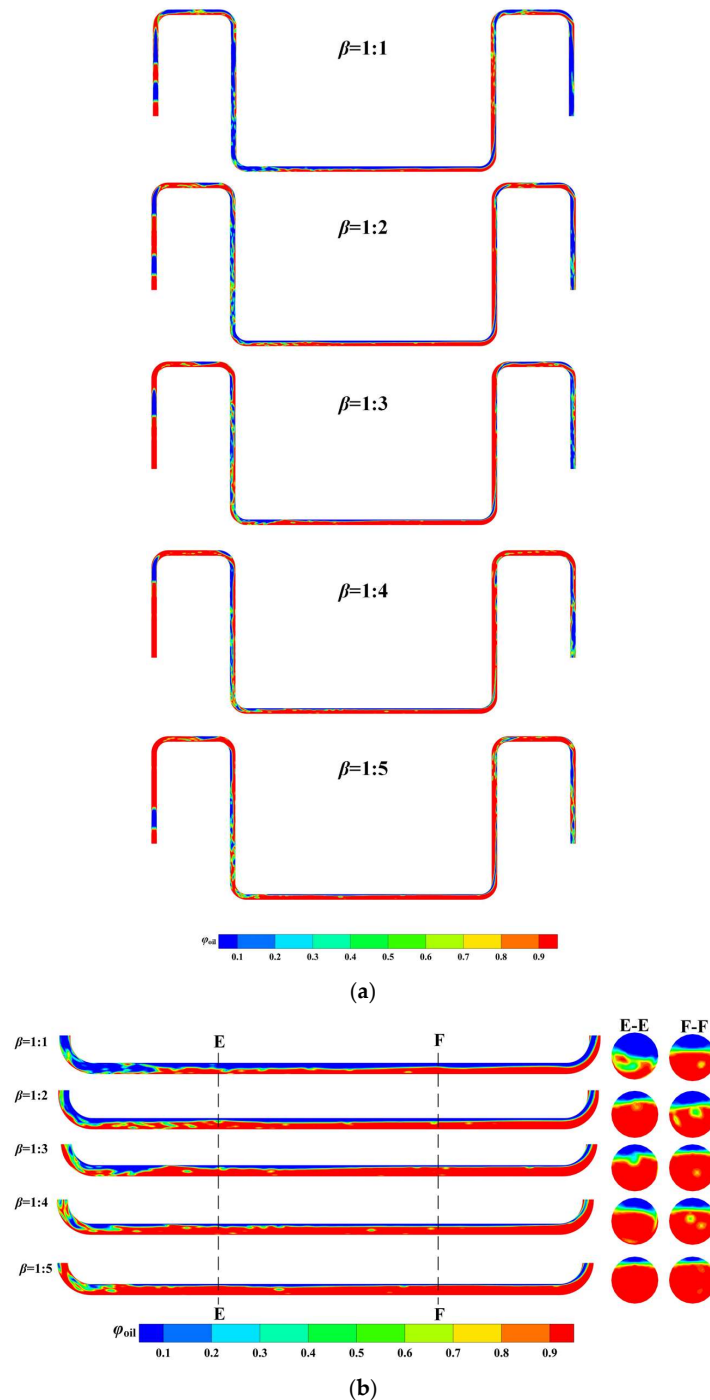
Figure 13. Comparison of flow regimes at different gas-liquid ratios, where φ_{gas} is the gas void fraction, β is the gas-liquid ratio, and E-E and F-F denote two selected cross-sections along the bottom horizontal tube: (**a**) flow regimes in the jumper when the periodically stable flow is achieved; (**b**) contours of oil volume fraction in the bottom tube and the zoom-in view of two considered cross-sections.
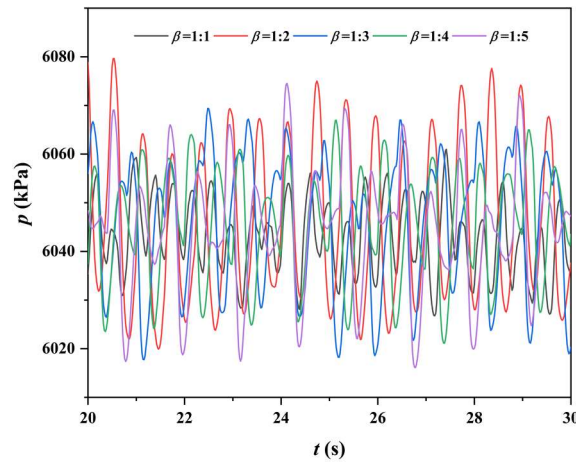
Figure 14. Comparison of the pressure (*p*) acting on Bend 3 at different gas-liquid ratios, where *β* is the gas-liquid ratio.
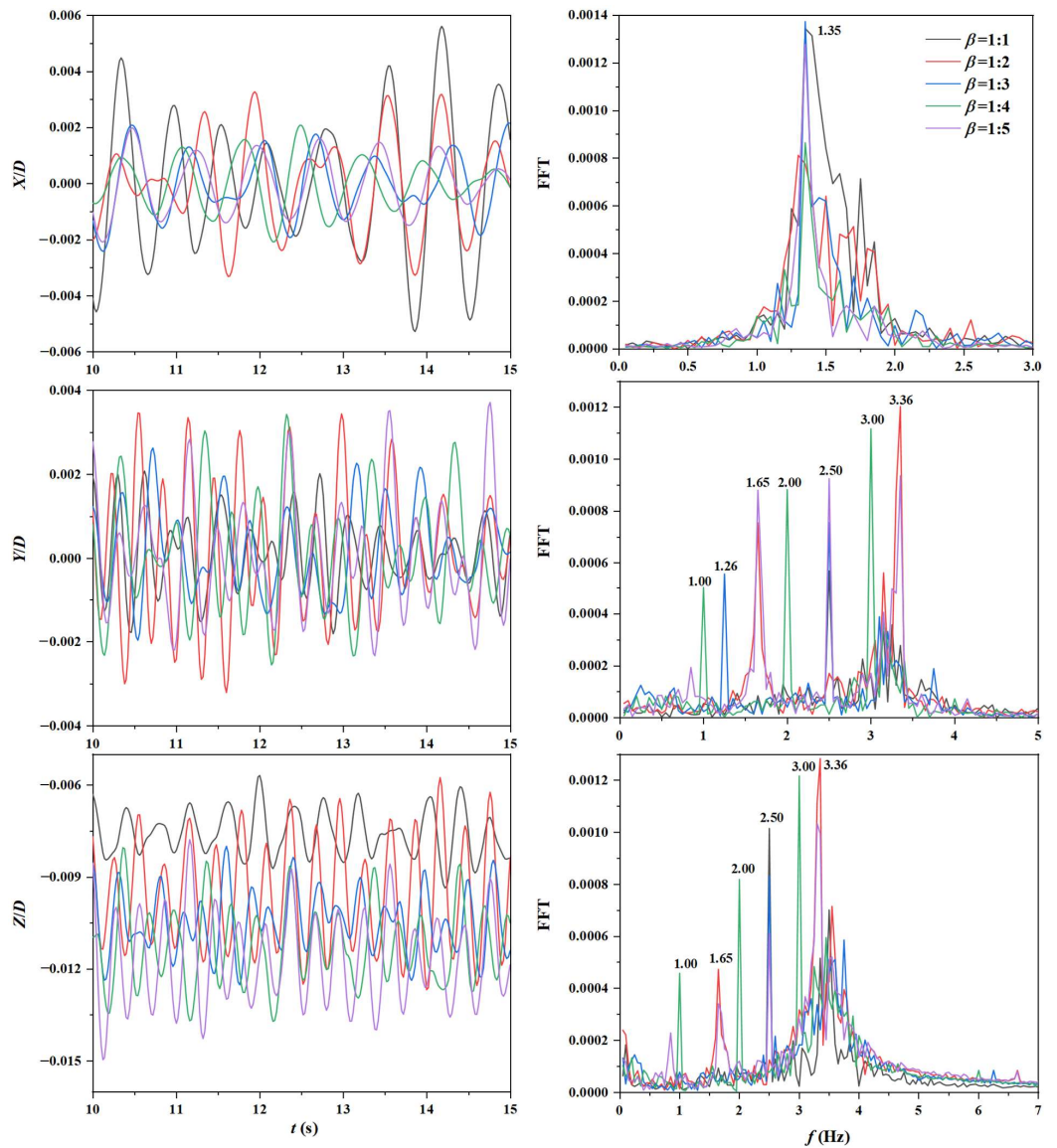

Figure 15. Comparison of the vibration response of the midspan of bottom horizontal span (Probe C) at different gas-liquid ratios, where *β* is the gas-liquid ratio, and *X/D*, *Y/D* and *Z/D* are the normalized displacements in the three directions.
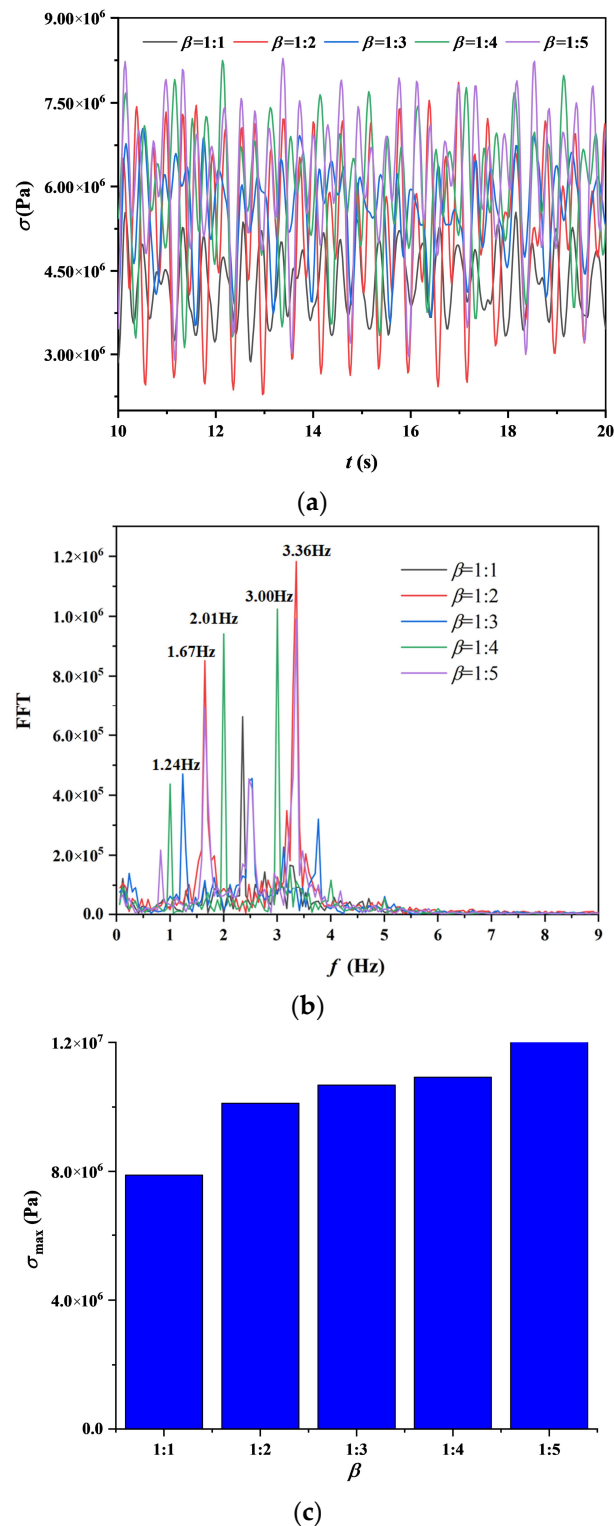
(a)

(b)

(c)

Figure 16. The stresses of Bend 5 at different gas-liquid ratios, where β is the gas-liquid ratio, σ_{max} is the maximum stress, σ is the structural stress, f is the fluctuation frequency and t is the flow time: (**a**) time series of structural stresses; (**b**) frequency spectra of structural stresses; (**c**) comparison of the maximum stress.

4.4. Effect of Inflow Mixture Velocity

In this section, the numerical results also apply for a rigid jumper. The variation of gas-liquid mixture velocity also results in the change of flow evolution in the jumper, as depicted in Figure 17. In the first upward tube, the length of oil slugs is elongated with

increasing v_m. After that, the flow pattern in the left horizontal span evolves from the wavy flow to the churn flow as v_m grows from 2 m/s to 6 m/s, attributed to the increased flow momentum. Subsequently, oil falls in a faster velocity with increasing v_m in the left downward tube, contributing to the flow regime transition from annular flow to churn flow. Such churn flow introduces a disturbance to the stratified flow in the bottom horizontal span. As a result, the flow pattern evolves into a wavy flow when v_m is increased to 6 m/s, and the gas-liquid interface fluctuates more violently. In contrast, the mixture flow in the right upward tube is stabilized as v_m increases, resulting in the transition from churn flow to annular flow. This is possibly the result of the increased upward kinetic energy that overcomes the action of gravity. The annular flow is maintained in the left half of the right horizontal span, and it changes into the aerated wavy flow in the right half. Then, the gas-liquid mixture drops in the right downward tube in an aerated slug flow at v_m = 6 m/s.

(a)

Figure 17. *Cont.*
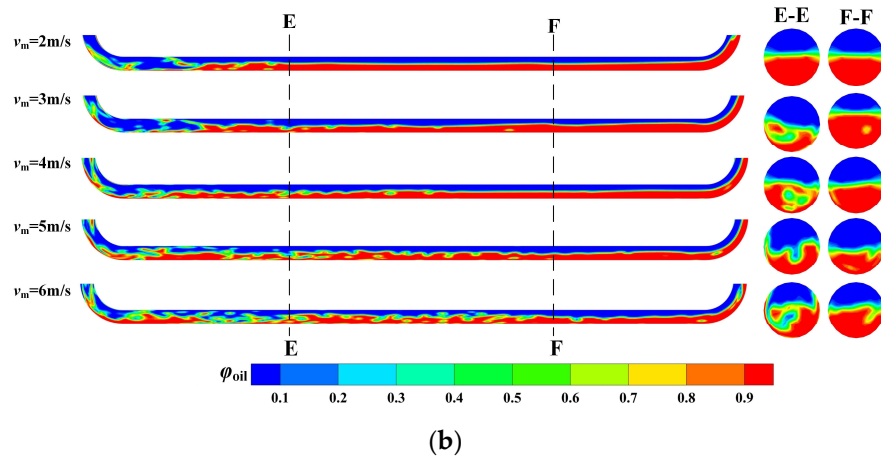
(b)
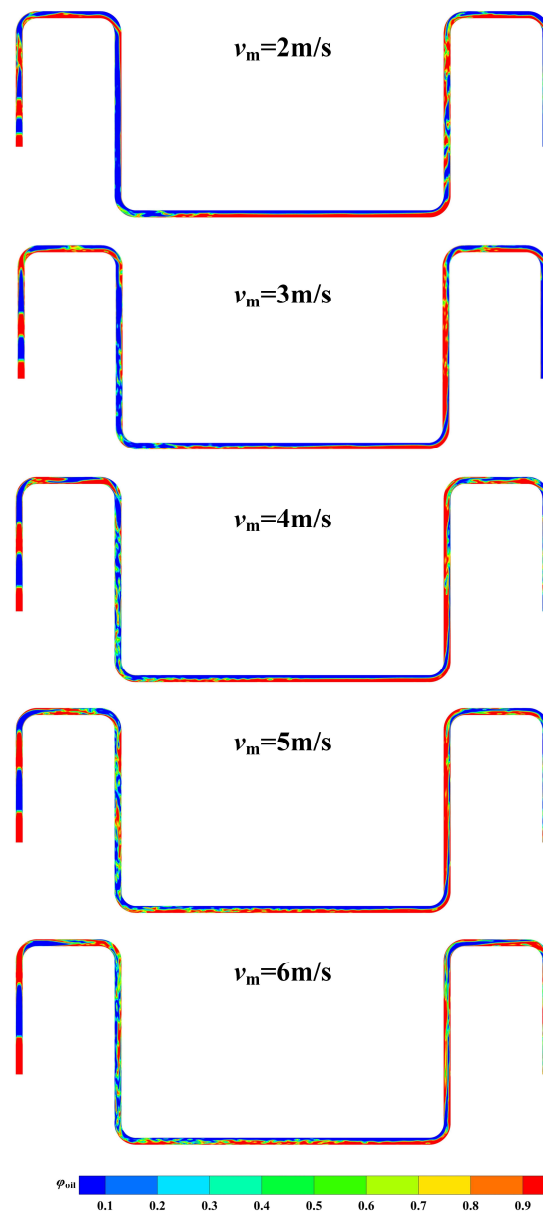
Figure 17. Comparison of flow regimes at different inlet velocities, where φ_{gas} is the gas void fraction, v_m is the mixture velocity, and E-E and F-F denote two selected cross-sections along the bottom horizontal tube: (**a**) flow regimes in the jumper when the periodically stable flow is achieved; (**b**) contours of oil volume fraction in the bottom tube and the zoom-in view of two considered cross-sections.

Due to the increased kinetic energy of the gas-liquid mixture, the pressure acting on Bend 3 is augmented with the increase of v_m, as shown in Figure 18. As compared to $v_m = 2$ m/s, the time-averaged pressure is increased by 12 kPa at $v_m = 6$ m/s, accompanied with a triple fluctuation amplitude. Accordingly, both the in-plane and out-of-plane responses are amplified with increasing v_m, as illustrated in Figure 19. The out-of-plane response amplitude is significantly augmented because the dominant frequency of 1.4 Hz is closer to the fundamental natural frequency. Due to the out-of-plane response, the maximum twist angle of 0.0127° occurs at the middle horizontal tube for $v_m = 6$ m/s. In contrast, the maximum twist angle of the two top pipe sections is less than 0.0016°. In comparison with the vertical response amplitude, the growth in the horizontal amplitude becomes more obvious as v_m grows from 2 m/s to 5 m/s. However, the amplitude difference between the cases of $v_m = 5$ m/s and $v_m = 6$ m/s is smaller than that of vertical oscillation. In general, the in-plane amplitude is nearly quadrupled when v_m increases from 2 m/s to 6 m/s. The dominant frequency of in-plane response is still approximately equal to the inflow slug flow frequency, while the secondary frequency is close to the fundamental natural one. Additionally, several higher frequencies participate in the in-plane response when v_m reaches 6 m/s, suggesting the influence of complicated flow evolution.
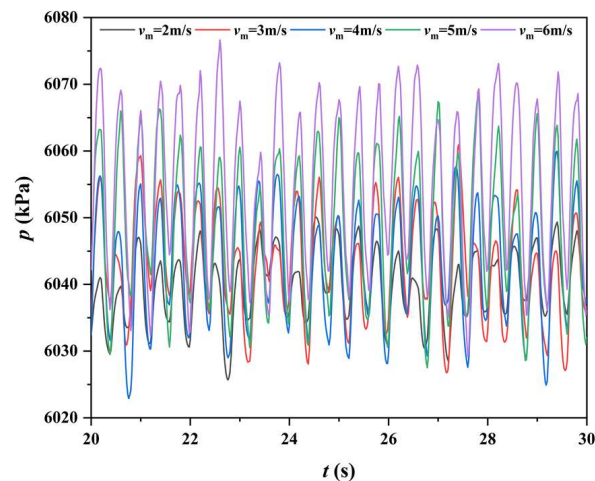

Figure 18. Comparison of the pressure (*p*) acting on Bend 3 at different mixture velocities, where v_m is the mixture velocity.
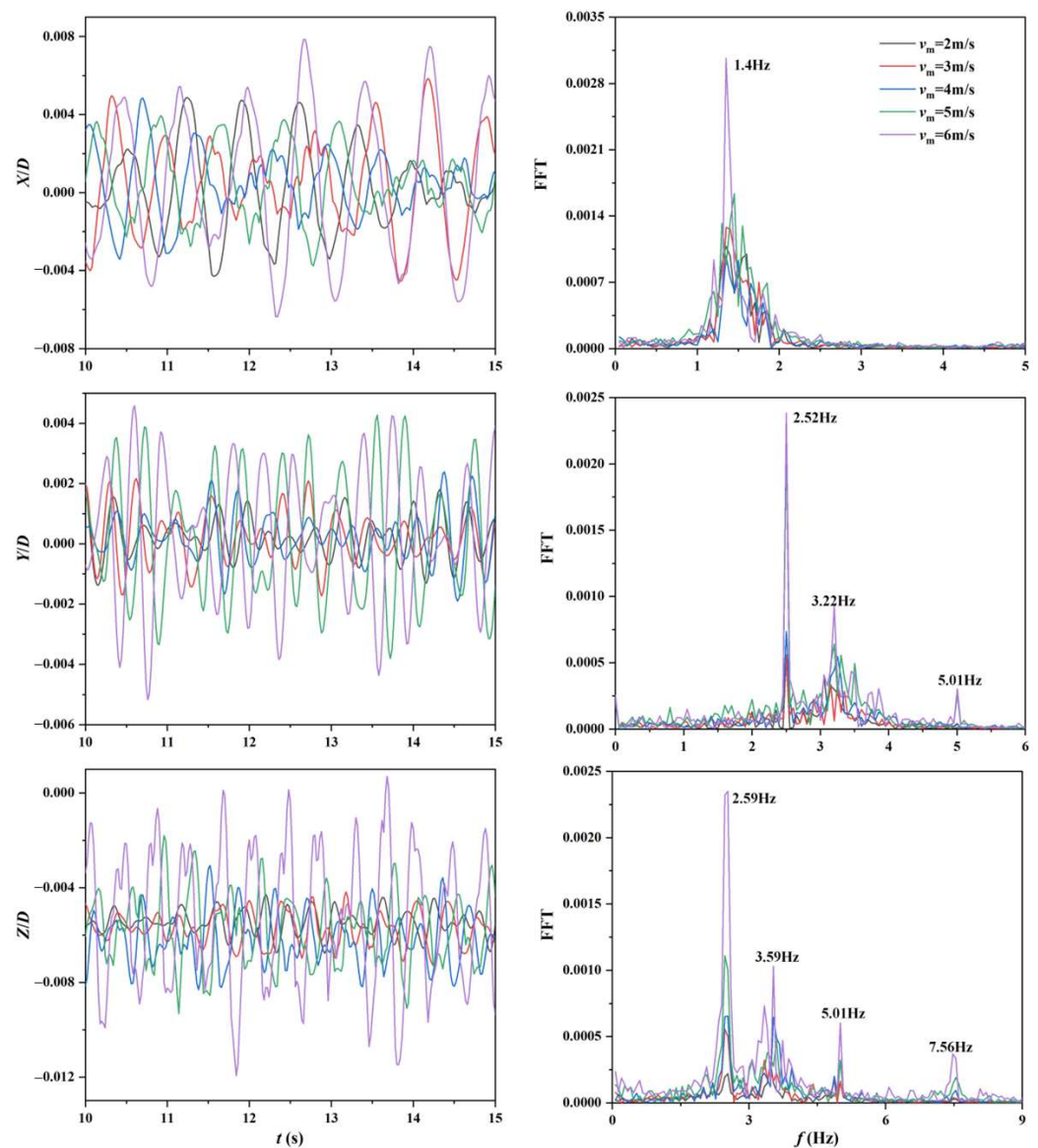
Figure 19. Comparison of the vibration response of the midspan of the bottom horizontal tube (Probe C) at different mixture velocities, where v_m is the mixture velocity, and X/D, Y/D and Z/D are the normalized displacements in the three directions.

Figure 20 compares the variation of the structural stresses of Bend 2 and Bend 5 with v_m. The maximum stress ($\sigma_{\max}$) of Bend 2 grows gradually with v_m, and is approximately doubled at $v_\mathrm{m} = 6$ m/s as compared to $v_\mathrm{m} = 2$ m/s. In contrast, Bend 5 does not undergo the monotonic increasing of $\sigma_{\max}$ with v_m. The maximum stress of Bend 5 is even slightly reduced as v_m increases from 4 m/s to 6 m/s. It is closely related to the flow evolution before and after this bend. At $v_\mathrm{m} \geq 4$ m/s, the flow patterns in both the right upward tube and right horizontal span are stabilized in comparison with $v_\mathrm{m} < 4$ m/s, as seen in Figure 17. Moreover, the gas accumulation at the bend is accelerated with increasing v_m, possibly contributing to the slight reduction of $\sigma_{\max}$. The fluctuation frequencies of the structural stresses of both Bend 2 and Bend 5 are approximately equal to the vibration frequencies of out-of-plane and vertical responses, further indicating the correlation between them.
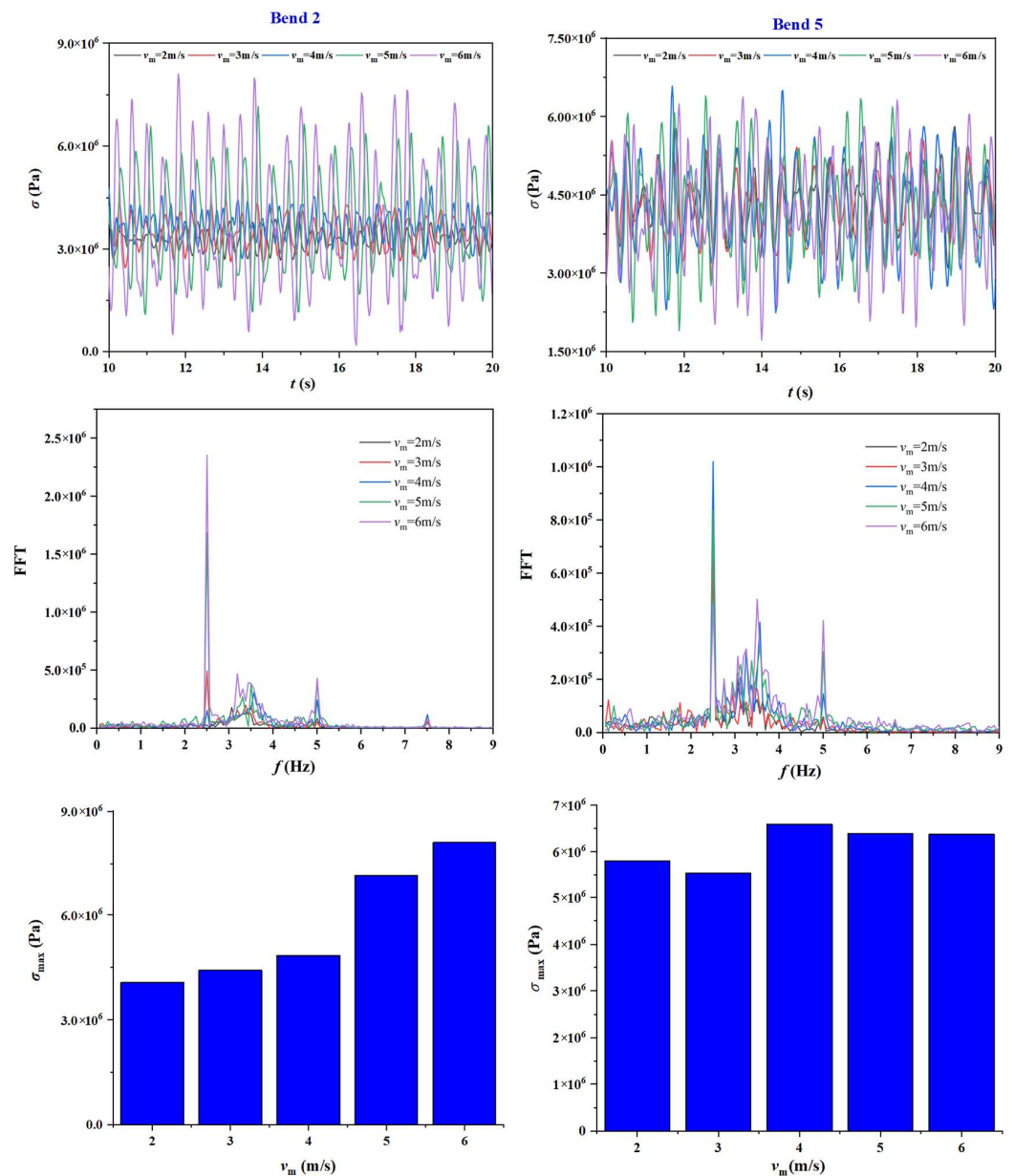
Figure 20. Comparison of the stresses of Bend 2 and Bend 5 at different mixture velocities, where v_m is the mixture velocity, σ_{max} is the maximum stress, σ is the structural stress, f is the fluctuation frequency and t is the flow time.

5. Conclusions

The present work numerically investigated the natural gas-oil two-phase flow evolution in an M-shaped subsea jumper and the resultant multiphase flow-induced vibration (MFIV) in a flow velocity range of 2 to 6 m/s with gas-liquid ratios ranging from 1:1 to 1:5. Based on the numerical results, the major conclusions are drawn as follows:

(1) The flow regime experiences a distinct adjustment after each turn of flow direction due mainly to the combination of centrifugal force, inertia force, gravity force and buoyant force. In the standard case (β = 1:1 and v_m = 3 m/s), the flow pattern successively presents slug flow, wavy flow, imperfect annular flow, stratified flow, churn flow, wavy flow and imperfect annular flow in the pipe sections along the jumper. Although the flow regime in a specific cross-section has no variation, the gas void fraction fluctuates periodically, suggesting the disturbance of the gas-liquid interface. The gas-liquid mixture development is significantly altered by changing either the gas-liquid ratio

or the mixture velocity. With reducing β or increasing v_{m}, the pattern evolves from annular flow to churn flow or aerated slug flow in the downward tubes. In contrast, the corresponding regime in the right upward tube shifts from churn flow to bubbly or annular flow as a result of stabilization. The small-amplitude oscillation of order of $10^{-3}D$ does not alter the flow pattern in pipe segments but stabilizes the mixture flow in the middle span and the subsequent upward tube.

(2) The pressure stresses acting on six bends fluctuate in multiple frequencies due to the occurrence of flow pattern transition and multi-frequency fluctuation of gas void fraction. Nevertheless, the dominant frequency of pressure fluctuation is approximately equal to the inflow slug frequency, indicating the close correlation between them. The flow evolution along the jumper introduces other secondary frequencies with increased allocated energy along the flow path. As a result of falling liquid impact, the third bend bears the maximum pressure stress. As β reduces from 1:1 to 1:5, the pressure acting on the third bend is augmented, which is also observed with the increase of v_{m} from 2 m/s to 6 m/s. In contrast, the bends close to both ends undergo larger structural stresses. The disturbance introduced by the pattern transition from churn flow to wavy flow contributes to the maximum fluctuation amplitude of structural stress of the fifth bend. The structural stress of this bend is amplified with the reduction of β, while presents a non-monotonic variation with v_{m} due to the flow evolution.

(3) Both the in-plane and out-of-plane responses of the jumper exhibit spatial-temporal variation characteristics. Due to the end constraints, the bends close to both ends experience negligible displacements in the vertical and out-of-plane directions. However, the horizontal displacements are identifiable for the two bends but in the opposite offset directions. The oscillation becomes prominent in the middle span and the connected bends. Furthermore, the out-of-plane response is more vigorous than the in-plane vibration. The largest out-of-plane amplitude as well as the maximum downward displacement occur at the midspan of the jumper, attributed to the concentrated energy at a single frequency close to the fundamental natural frequency. The in-plane response is dominated by the inflow slug frequency, owing to the occurrence of flow turns in the jumper plane. As β reduces, the out-of-plane response of the midspan of the jumper is suppressed while the in-plane response is enhanced. Moreover, the multi-frequency competition becomes more intense in the jumper plane. By contrary, both the in-plane and out-of-plane oscillations are enhanced with increasing v_{m}.

In summary, the vibration response of a jumper is closely related to the flow evolution and the pressure fluctuation. The bends close to jumper ends bear larger structural stresses, which should be paid attention to in practice. Further extensive studies are required to systematically figure out the effects of structural material properties and dimension parameters, fluid properties, as well as a broader range of gas-liquid ratios and flow rates on the MFIV response and to uncover the associated physics.

References

1. Sun, L.; Kang, Y. Installation strength analysis of subsea flowline jumpers. *J. Mar. Sci. Appl.* **2015**, *14*, 316–326. [CrossRef]
2. Zhu, H.J.; Gao, Y.; Zhao, H.L. Coupling vibration response of a curved flexible riser under the combination of internal slug flow and external shear current. *J. Fluids Struct.* **2019**, *91*, 102724. [CrossRef]
3. Zhu, H.J.; Hu, J.; Gao, Y.; Zhao, H.L.; Xu, W.H. Spatial-temporal mode transition in vortex-induced vibration of catenary flexible riser. *J. Fluid Struct.* **2021**, *102*, 103234. [CrossRef]
4. Lu, Y.; Liang, C.; Manzano-Ruiz, J.J.; Janardhanan, K.; Perng, Y. Flow-Induced Vibration in Subsea Jumper Subject to Downstream Slug and Ocean Current. *J. Offshore Mech. Arct. Eng.* **2016**, *138*, 021302. [CrossRef]
5. Van der Heijden, B.; Smienk, H.; Metrikine, A.V. Fatigue analysis of subsea jumpers due to slug flow. In Proceedings of the 33rd International Conference on Ocean, Offshore and Arctic Engineering, San Francisco, CA, USA, 8–13 June 2014.
6. Tamunodienye, I.; Zhu, H.J.; Srinil, N. 3-D numerical simulations of liquid-gas flow development in subsea jumper with variable flow rates. In Proceedings of the 2020 International Conference on Ships and Offshore Structures, Glasgow, UK, 1–4 September 2020.
7. Al-Ruhaimani, F.; Pereyra, E.; Sarica, C.; Al-Safran, E.; Chung, S.; Torres, C. A study on the effect of high liquid viscosity on slug flow characteristics in upward vertical flow. *J. Petrol. Sci. Eng.* **2018**, *161*, 128–146. [CrossRef]
8. Babakhani Dehkordi, P.; Colombo, L.P.M.; Mohammadian, E.; Arnone, D.; Azdarpou, A.; Sotgia, G. Study of viscous oil-water-gas slug flow in a horizontal pipe. *J. Petrol. Sci. Eng.* **2019**, *178*, 1–13. [CrossRef]
9. Pouraria, H.; Seo, J.K.; Paik, J.K. Numerical study of erosion in critical components of subsea pipeline: Tees vs bends. *Ships Offshore Struct.* **2016**, *12*, 233–243. [CrossRef]
10. Hossain, M.; Chinenye-Kanu, N.M.; Droubi, G.M.; Islam, S.Z. Investigation of slug-churn flow induced transient excitation forces at pipe bend. *J. Fluids Struct.* **2019**, *91*, 102733. [CrossRef]
11. Bakkouch, M.; Minguez, M. Riser base jumper slugging analysis by CFD simulations. In Proceedings of the 32nd International Conference on Ocean, Offshore and Arctic Engineering, Nantes, France, 8–13 June 2013.
12. Zhu, H.; Gao, Y.; Zhao, H.L. Experimental investigation on the flow-induced vibration of a free-hanging flexible riser by internal unstable hydrodynamic slug flow. *Ocean Eng.* **2018**, *164*, 488–507. [CrossRef]
13. Zhu, H.; Gao, Y.; Srinil, N.; Bao, Y. Mode switching and standing-travelling waves in slug flow-induced vibration of catenary riser. *J. Petrol. Sci. Eng.* **2021**, *203*, 108310. [CrossRef]
14. Chica, L.; Pascali, R.; Jukes, P.; Ozturk, B.; Gamino, M.; Smith, K. Detailed FSI analysis methodology for subsea piping components. In Proceedings of the 31st International Conference on Ocean, Offshore and Arctic Engineering, Rio de Janeiro, Brazil, 1–6 July 2012.
15. Elyyan, M.A.; Perng, Y.Y.; Doan, M. Fluid-structure interaction modeling of subsea jumper pipe. In Proceedings of the 33rd International Conference on Ocean, Offshore and Arctic Engineering, San Francisco, CA, USA, 8–13 June 2014.
16. Zhu, H.; Gao, Y.; Hu, J.; Zhao, H.; Bao, Y. Temporal-spatial mode competition in slug-flow induced vibration of catenary flexible riser in both in plane and out of plane. *Appl. Ocean Res.* **2022**, *119*, 103017. [CrossRef]
17. Jia, D. Slug flow induced vibration in a pipeline span, a jumper, and a riser section. In Proceedings of the 2012 Offshore Technology Conference, Houston, TX, USA, 30 April–3 May 2012.
18. Jia, D. Effect of boundary conditions, flow rate, slug length, and slug frequency on slug flow induced vibration in a pipeline span. In Proceedings of the 2013 Offshore Technology Conference, Houston, TX, USA, 6–9 May 2013.
19. Pontaza, J.P.; Menon, R.G. Flow-induced vibrations of subsea jumpers due to internal multi-phase flow. In Proceedings of the 30th International Conference on Ocean, Offshore and Arctic Engineering, Rotterdam, The Netherlands, 19–24 June 2011.
20. Dukler, A.E.; Maron, D.M.; Brauner, N. A physical model for predicting the minimum stable slug length. *Chem. Eng. Sci.* **1985**, *40*, 1379–1385. [CrossRef]
21. Staurland, G.; Aamodt, M. Designing offshore pipeline systems divided into sections of different design pressures. In Proceedings of the 2004 International Pipeline Conference, Calgary, AB, Canada, 4–8 October 2004; Volumes 1–3, pp. 1935–1943.
22. Pijl, S.P.V.D.; Segal, A.; Vuik, C. A mass conserving level set (MCLS) method for modeling of multi-phase flows. *Int. J. Numer. Meth. Fluids* **2005**, *47*, 339–361. [CrossRef]
23. Abdulkadir, M.; Hernandez-Perez, V.; Lo, S.; Lowndes, I.; Azzopardi, B.J. Comparison of experimental and computational fluid dynamics (CFD) studies of slug flow in a vertical riser. *Exp. Therm. Fluid Sci.* **2015**, *68*, 468–483. [CrossRef]
24. Araujo, J.D.P.; Miranda, J.M.; Campos, J.B.L.M. CFD study of the hydrodynamics of slug flow systems: Interaction between consecutive taylor bubbles. *Int. J. Chem. React. Eng.* **2015**, *13*, 541–549. [CrossRef]
25. Alfonsi, G. Reynolds-averaged Navier-Stokes equations for turbulence modeling. *Appl. Mech. Rev.* **2009**, *62*, 040802. [CrossRef]
26. Ishii, M.; Hibiki, T. *Thermo-Fluid Dynamics of Two-Phase Flow*; Springer: New York, NY, USA, 2010.
27. Zhu, H.; Lin, P.; Pan, Q. A CFD (computational fluid dynamic) simulation for oil leakage from damaged submarine pipeline. *Energy* **2014**, *64*, 887–899. [CrossRef]
28. Orszag, S.A.; Yakhot, V.; Flannery, W.S.; Boysan, F.; Choudhury, D.; Maruzewski, J.; Patel, B. Renormalization group modeling and turbulence simulations. In Proceedings of the International Conference on Near-Wall Turbulent Flows, Tempe, AZ, USA, 15–17 March 1993.
29. Yakhot, V.; Orszag, S.A.; Thangam, S.; Gatski, T.B.; Speziale, C.G. Development of turbulence models for shear flows by a double expansion technique. *Phys. Fluids A* **1992**, *4*, 1510–1520. [CrossRef]

30. Barth, T.J.; Jespersen, D. The design and application of upwind schemes on unstructured meshes. Technical Report AIAA-89-0366. In Proceedings of the AIAA 27th Aerospace Sciences Meeting, Reno, NV, USA, 9–12 January 1989.

31. Hoff, C.; Hughes, T.J.R.; Hulbert, G.; Pahl, P.J. Extended comparison of the Hilber-Hughes-Taylor α-method and the θ1-method. Computer Meth. *Appl. Mech. Eng.* **1989**, *76*, 87–93. [CrossRef]

32. Deng, L.; Zhang, Y.; Kennedy, D. Dynamics of 3D sliding beams undergoing large overall motions. Commun. *Nonlinear Sci. Numer. Sim.* **2021**, *3*, 105778. [CrossRef]

33. Bamidele, O.E.; Ahmed, W.H.; Hassan, M. Characterizing two-phase flow-induced vibration in piping structures with U-bends. *Int. J. Multiphase Flow.* **2022**, *151*, 104042. [CrossRef]